

UC San Diego

UC San Diego Previously Published Works

Title

Machine learning for daily forecasts of Arctic sea-ice motion: an attribution assessment of model predictive skill

Permalink

<https://escholarship.org/uc/item/2t59n4jx>

Authors

Hoffman, Lauren
Mazloff, Matthew R
Gille, Sarah T
[et al.](#)

Publication Date

2023-08-17

DOI

10.1175/aies-d-23-0004.1

Copyright Information

This work is made available under the terms of a Creative Commons Attribution License, available at <https://creativecommons.org/licenses/by/4.0/>

Peer reviewed

1 **Machine learning for daily forecasts of Arctic sea-ice motion: an attribution**
2 **assessment of model predictive skill.**

3 Lauren Hoffman,^a Matthew R. Mazloff,^a Sarah T. Gille,^a Donata Giglio,^b Cecilia M. Bitz,^c
4 Patrick Heimbach,^d Kayli Matsuyoshi,^a

5 ^a *Scripps Institution of Oceanography, University of California, San Diego, California, USA*

6 ^b *University of Colorado Boulder, Boulder, Colorado, USA* ^c *University of Washington, Seattle,*

7 *Washington, USA* ^d *The University of Texas at Austin, Austin, Texas, USA*

8 *Corresponding author:* Lauren Hoffman, lahoffma@eng.ucsd.edu

9 ABSTRACT: Physics-based simulations of Arctic sea ice are highly complex, involving transport
10 between different phases, length scales, and time scales. Resultantly, numerical simulations of
11 sea-ice dynamics have a high computational cost and model uncertainty. We employ data-driven
12 machine learning (ML) to make predictions of sea-ice motion. The ML models are built to predict
13 present-day sea-ice velocity given present-day wind velocity and previous-day sea-ice concentra-
14 tion and velocity. Models are trained using reanalysis winds and satellite-derived sea-ice properties.
15 We compare the predictions of three different models: persistence (PS), linear regression (LR),
16 and convolutional neural network (CNN). We quantify the spatio-temporal variability of the corre-
17 lation between observations and the statistical model predictions. Additionally, we analyze model
18 performance in comparison to variability in properties related to ice motion (wind velocity, ice
19 velocity, ice concentration, distance from coast, bathymetric depth) to understand the processes
20 related to decreases in model performance. Results indicate that a CNN makes skillful predictions
21 of daily sea-ice velocity with a correlation up to 0.81 between predicted and observed sea-ice
22 velocity, while the LR and PS implementations exhibit correlations of 0.78 and 0.69, respectively.
23 The correlation varies spatially and seasonally; lower values occur in shallow coastal regions and
24 during times of minimum sea-ice extent. LR parameter analysis indicates that wind velocity plays
25 the largest role in predicting sea-ice velocity on one-day time scales, particularly in the central
26 Arctic. Regions where wind velocity has the largest LR parameter are regions where the CNN has
27 higher predictive skill than the LR.

28 SIGNIFICANCE STATEMENT: We build and evaluate different machine learning (ML) mod-
29 els that make one-day predictions of Arctic sea-ice velocity using present-day wind velocity and
30 previous-day ice concentration and ice velocity. We find that models that incorporate non-linear
31 relationships between inputs (a neural network) capture important information (i.e. have a higher
32 correlation between observations and predictions than linear and persistence models). This perfor-
33 mance enhancement occurs primarily in deeper regions of the central Arctic where wind speed is
34 the dominant predictor of ice motion. Understanding where these models benefit from increased
35 complexity is important because future work will use ML to elucidate physically meaningful rela-
36 tionships within the data, looking at how the relationship between wind and ice velocity is changing
37 as the ice melts.

38 **1. Introduction**

39 Sea-ice cover in the Arctic has been diminishing since the beginning of the satellite record.
40 (Serreze et al. 2007; Stroeve et al. 2012; Stroeve and Notz 2018; Thoman et al. 2022). Negative
41 trends in sea-ice concentration, thickness, and multiyear ice coverage (Carmack et al. 2015) have
42 been reported throughout the Arctic, whereas the length of the melt season, drift speeds, and
43 deformation rates are increasing (Stroeve and Notz 2018; Rampal et al. 2009; Onarheim et al.
44 2018). Climate model simulations indicate a substantial likelihood that the Arctic Ocean will
45 become largely ice free during September by 2100 if warming exceeds 2°C (Stroeve and Notz
46 2018; Notz and Stroeve 2018; Jahn 2018; Meredith et al. 2019). Transition to thinner and more
47 fragile ice will have widespread environmental, geopolitical, and logistical impacts, including
48 potential for new increased maritime activity (Bennett et al. 2020; Crawford et al. 2021; Cao et al.
49 2022), with which comes the need to know where sea-ice is and the need for skillful predictions
50 of where it will be. In this study we contribute to addressing these issues by assessing the skill of
51 machine learning models in making one-day predictions of sea-ice motion. We design these models
52 to predict present-day ice motion based on previous-day observations, and show proof-of-concept
53 for applications in operational forecasting that would allow information about the ice state to be
54 obtained before satellite retrievals are processed. Additionally, we explore the extent to which
55 these ML models will have enough skill to be used to represent the dynamical component of sea
56 ice in a simulation framework that provides nowcasting of the state of Arctic sea ice.

57 Predictions of sea-ice motion have almost exclusively been attempted with numerical prediction
58 models (Petrou and Tian 2019). While these state-of-the-art physics-based models for sea-ice
59 prove useful, their inherent complexity comes with a high computational cost (Hunke et al. 2020).
60 There are also several sources of uncertainty, including large sensitivity to initial conditions and
61 physical assumptions (Blanchard-Wrigglesworth et al. 2015). In contrast to physics-based models,
62 machine learning is emerging as a powerful tool for applications in the geosciences in cases where
63 large volumes of data are available (Hsieh and Tang 1998; Toms et al. 2020). Machine learning
64 predictions are driven by data and therefore do not depend on assumptions imposed on physical
65 constraints. Although these constraints are crucial for some applications (e.g. where mass, heat,
66 and momentum need to be conserved), in other applications they introduce additional uncertainty
67 and complexity with little scientific benefit. While simple forms of machine learning (e.g. linear
68 regression) have been commonly used in the geosciences, more advanced deep learning models
69 (e.g. neural networks) have the potential to further elucidate physically meaningful relationships
70 within data (McGovern et al. 2019; Toms et al. 2020). In this study, we assess the viability of using
71 a neural network as a surrogate model to parameterize sea-ice motion in a numerical model setting
72 on one-day time scales.

73 Machine learning models for sea-ice have been applied to improve estimates of ice properties
74 from satellite remote sensing (Lee et al. 2016; Dumitru et al. 2019), to predict and understand
75 sea-ice concentration on different time scales (Kim et al. 2020; Li et al. 2021; Andersson et al.
76 2021), and to make predictions of sea-ice motion (Petrou and Tian 2019; Zhai and Bitz 2021).
77 ML models have been successful at improving predictions of sea-ice properties in comparison to
78 state-of-the-art dynamical models. For example, the deep learning model IceNet outperformed
79 the SEAS5 dynamical model from the European Centre for Medium-Range Weather Forecasts
80 (ECMWF) for lead times greater than one month when making seasonal forecasts of summer ice
81 (Andersson et al. 2021). Additionally, a CNN designed to make one-day predictions of ice motion
82 showed higher correlations with satellite observations than CICE5, a leading physics-based model
83 for sea ice (Zhai and Bitz 2021). The high performance of this CNN provides evidence that a CNN
84 would be an effective surrogate model to replace the sea ice dynamical component of a numerical
85 model for short-time-scale predictions. We build upon the work of Zhai and Bitz (2021) by further

86 analyzing the nuances in the performance of a CNN in predicting ice motion, and by building the
87 case for its use over a conventional linear regression approach.

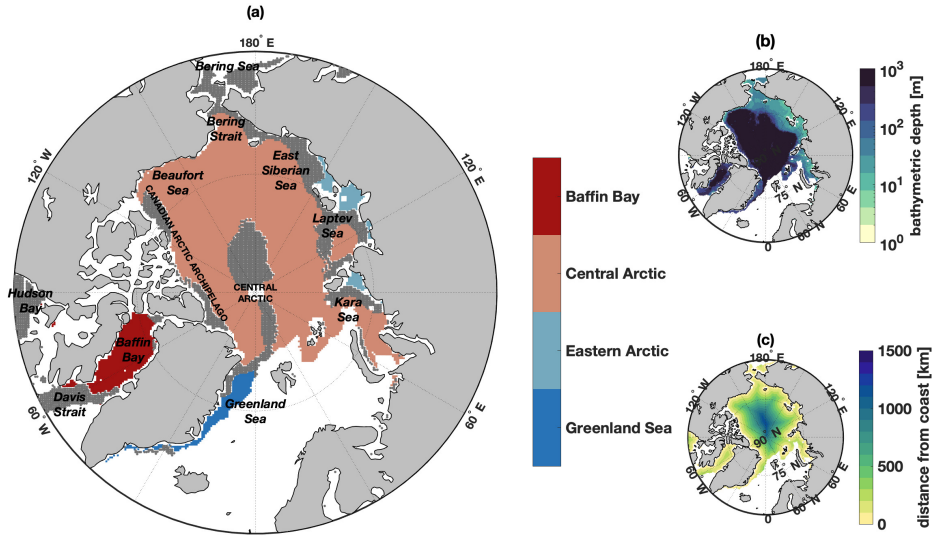
88 We apply three different models, including persistence (PS), linear regression (LR), and convolu-
89 tional neural network (CNN) to make predictions of sea-ice motion. In comparison to the other two
90 models, a CNN has the benefits of incorporating spatial information and non-linear relationships
91 between the inputs into its predictions. We build a CNN that has a similar architecture to that of
92 Zhai and Bitz (2021) (differences are noted in the supplementary information, Table S1) and that is
93 trained on the same input and output data. Our models show similar performances in making one-
94 day predictions of sea-ice motion (Table S1). We expand on previous work by putting an emphasis
95 on understanding the spatial and temporal variability in performance of the different models and
96 how it is related to various properties of the ice. We divide the Arctic into four geographic regions
97 (Fig. 1) based on the differences in skill between the CNN and LR models, and we analyze model
98 performance within each.

109 2. Background

110 Sea-ice motion, as described by the momentum equation (Equation 1), is determined from a
111 balance of the momentum tendency ($\frac{D}{Dt}(m\vec{u})$) with drag from the atmosphere ($\vec{\tau}_a$) and ocean ($\vec{\tau}_w$),
112 the Coriolis force ($m f \hat{k} \times \vec{u}$), the ocean surface tilt ($mg\nabla H$), and the internal ice stress ($\nabla \cdot \sigma$)
113 (Olason and Notz 2014; Feltham 2008). The term on the left represents the total derivative of
114 mass, m times velocity, \vec{u} :

$$\frac{D}{Dt}(m\vec{u}) = \vec{\tau}_a + \vec{\tau}_w - m f \hat{k} \times \vec{u} - mg\nabla H - \nabla \cdot \sigma. \quad (1)$$

115 Changes in external forcing (i.e. winds, currents, radiation, etc.) influence the geometric and
116 mechanical properties of the ice (thickness distribution, mass, strength, drag coefficients, etc.),
117 which ultimately impact ice motion and deformation (Untersteiner et al. 2007). The American-
118 Canadian Arctic Ice Dynamics Joint Experiment (AIDJEX) of 1970-1978 was one of the first
119 major studies aimed at developing a comprehensive model of sea-ice motion under the influences
120 of the ocean and atmosphere (Maykut et al. 1972; Untersteiner et al. 2007). Using data from the
121 AIDJEX experiments, Thorndike and Colony (1982) introduced a relationship between sea-ice
122 velocity and geostrophic wind that explained up to 70% of the variance in sea-ice velocity in the



99 FIG. 1. Maps showing (a) spatial divisions (Greenland Sea, Eastern Arctic, Central Arctic, and Baffin Bay),
 100 (b) bathymetric depth [m] (note logarithmic scaling), and (c) the distance from coast [km]. Spatial divisions
 101 are based on overall performance of the CNN model and the difference between the performance of the CNN
 102 and LR models. The four divisions represent regions of: variable model performance and $corr_{LR} \gg corr_{CNN}$
 103 (Greenland Sea, dark blue), low model performance and $corr_{LR} > corr_{CNN}$ (Eastern Arctic, light blue), high
 104 model performance and $corr_{LR} < corr_{CNN}$ (Central Arctic, light red), and variable model performance and
 105 $corr_{LR} \ll corr_{CNN}$ (Baffin Bay, dark red). Gray shading represents areas where the difference in correlation
 106 between the CNN and LR is not statistically significant or areas that are not included within this analysis. Data
 107 are not shown in regions where the ice concentration is zero or the satellite retrievals are absent for more than
 108 20% of the year.

123 central Arctic. This relationship describes ice that is subject to high wind speeds on time scales of
 124 days to months. In this relationship, sea-ice velocity is related to geostrophic wind velocity through
 125 a speed reduction factor (the wind factor) and a turning angle, after removal of the long-term mean
 126 ice velocity field. In the absence of a steady ocean current, sea-ice moved about 8° to the right
 127 of the geostrophic wind at about 0.008 times the speed. This model is less successful for areas
 128 within 400 km of the coast, where stress gradients within the ice become more important due to
 129 the restriction of ice motion by geographical features (Thorndike and Colony 1982).

130 The internal stress gradient also depends on factors including the magnitude of the wind speed,
 131 ice concentration, and ice thickness. Ice with high values for thickness and concentration may have

132 large stress gradients, which can result in a smaller dependence on wind. Conversely, ice with
133 smaller stress gradients (low thickness and concentration) is found to have higher dependencies on
134 wind (Hibler 1979). Decreases in correlation between wind and ice motion near the coast have
135 often been attributed to ice stresses (Thorndike and Colony 1982; Kimura and Wakatsuchi 2000;
136 Hibler 1979).

137 A relationship between ice motion and geostrophic wind was also examined by Kimura and
138 Wakatsuchi (2000) and by Maeda et al. (2020), using sea-ice motion derived from satellite products
139 and geostrophic wind derived from the sea-level pressure data from ERA Interim Reanalysis data
140 produced by European Centre for Medium-Range Weather Forecasts (ECMWF) on 2.5° and 0.75°
141 grids, respectively. In these studies, geostrophic wind was generally found to explain 70% of the
142 variance in sea-ice velocity, with 60–90% of the variance explained in the central Arctic, and
143 up to 40% in coastal regions (Fig. 3 in Maeda et al. (2020)). In addition to spatial variability,
144 seasonal variations in the speed reduction factor and turning angle have been reported (Thorndike
145 and Colony 1982; Kimura and Wakatsuchi 2000; Kwok et al. 2013; Maeda et al. 2020).

146 **3. Data**

147 In our analysis, models are trained to make one-day predictions of sea-ice velocity given present-
148 day wind velocity, previous-day sea-ice concentration, and previous-day sea-ice velocity from
149 various satellite and reanalysis sources, during 1989–2021. Using present-day wind as a predictor
150 of present-day sea-ice velocity incorporates information that gives the model intrinsic skill. This
151 approach is appropriate for the objective to make predictions on one-day time scales. We opt not
152 to detrend to avoid contaminating the data with spurious removals. However, we do find that the
153 model performance does not have any significant changes when run on data with the seasonal cycle
154 removed (not shown). Processed data and methods for obtaining and processing raw data are made
155 available by (Hoffman et al. 2023).

156 The ice velocity and concentration data are available from 25 October 1978 to 31 December
157 2021. However, evaluation of the uncertainty metrics for the Polar Pathfinder ice motion product
158 shows a change in the error fields starting in the summer of 1987 (Figure S1) due to a difference
159 in the sampling period when switching from using Scanning Multichannel Microwave Radiometer
160 (SMMR, 48hr sampling period) to Special Sensor Microwave/Imagers (SSM/Is, 24hr sampling

161 period) for brightness temperature (Tschudi et al. 2020). Additionally, ice concentration data from
162 the Nimbus-7 passive microwave are only available every other day until 1987, and there is a gap
163 in availability of the sea ice concentration data from 03 December 1987 to 12 January 1988. Thus,
164 for consistency in the stability of the observation systems and the quantity of data used from each
165 year, we use data from 1989-2021 to build our models. We use the satellite and reanalysis sources
166 discussed below for consistency with Zhai and Bitz (2021). However, in comparison, we make a
167 slight extension to the temporal subset of data over which the model is trained and tested.

168 *a. Sea-Ice Velocity: Polar Pathfinder Version 4 Daily Sea Ice Motion vectors (PP)*

169 The Polar Pathfinder product (PP; Tschudi et al. 2019) provides daily sea-ice motion vectors at
170 a spatial resolution of 25 km in the Equal-Area Scalable Earth (EASE)-grid. The EASE-grid was
171 defined by the NOAA/NASA Polar Pathfinder Program to support standardized spatial comparisons
172 from gridded, satellite microwave data. In polar regions, the EASE-Grid takes the form of Lambert
173 azimuthal equal-area projections that accurately represent area in all regions of the global sphere.
174 (Brodzik et al. 2012). This data set is informed by optimal interpolation of a combination of
175 observations from passive microwave inputs, buoys, and NCEP/NCAR reanalysis winds. The PP
176 dataset relies on wind because during the summer, passive microwave and buoy sources become
177 unreliable for melting ice (Tschudi et al. 2020). For wind-derived ice motions, ice is assumed
178 to move at $\sim 1\%$ of the wind speed and in the direction of the wind, based on the estimate from
179 Thorndike and Colony (1982). An estimated uncertainty map is also provided, which we use for
180 comparison when evaluating our models. We were unable to obtain a dataset that is independent
181 from the PP product to validate the use of the PP for this case. We did find high correlation between
182 the PP and the Ice-Tethered Profiler data (not shown), but these observations were used to create
183 the PP product. Wang et al. (2022) found the PP to have low accuracy in speed, but high accuracy
184 in angle in comparison to eleven other satellite products when evaluated against measurements
185 from buoys from the International Arctic Buoy Program (IABP) and the Multidisciplinary drifting
186 Observatory for the Study of Arctic Climate (MOSAiC).

187 *b. Sea-Ice Concentration: Nimbus-7 SMMR and DMSP SSM/I-SSMIS Passive Microwave Data*

188 The passive microwave sea-ice concentration product (Cavalieri et al. 1996) is generated from
189 brightness temperature data derived from various sensors (SMMR, DMSP and SSM/I-SSMIS).
190 This product provides daily measurements of sea-ice concentrations (fraction of ocean area covered
191 by sea ice in each grid cell) in a 25×25 km polar stereographic projection. Here we re-grid to the
192 25-km EASE-grid for consistency with other ML model inputs. An intercomparison study of 10
193 satellite passive microwave sea-ice concentration data sets by Kern et al. (2019) found that while
194 the Nimbus-7 product used in this work showed the largest difference between other products,
195 all 10 products compared reasonably well to ship-based observations. Additionally, the Nimbus-7
196 product used in this study showed less than a 7% deviation from all other products from November–
197 June, and less than a 15% deviation from July–October when comparing the monthly mean values
198 of sea-ice concentration among the 10 products from June 2002 to September 2011. The product
199 used in this study was also found to have a negative bias in sea-ice concentration throughout the
200 Arctic in comparison to the ensemble mean of the 10 products (Fig. 8 from Kern et al. (2019)).
201 While this negative bias was particularly large in the peripheral seas, it was close to zero (i.e. <
202 6%) in the region of study of this work.

203 *c. Wind Velocity: Japanese 55-year Reanalysis derived for ocean-ice models (JRA55-do)*

204 The Japanese Meteorological Agency 55-year atmospheric reanalysis based surface dataset for
205 driving ocean-sea ice models (JRA55-do) is used to prescribe wind velocity (Tsujino et al. 2018).
206 Based on the JRA55 (Kobayashi et al. 2015), the JRA55-do is derived for use in ocean simulations,
207 with surface fields adjusted relative to satellite climatological winds (SSM/I and QuikSCAT) using
208 a spatially varying wind factor for wind speed and EOF analysis for wind direction (Tsujino et al.
209 2018). The JRA55-do better matches satellite wind fields in coastal areas than do other reanalysis
210 products (Taboda et al. 2019). The JRA55-do provides 3-hourly estimates of total wind velocity
211 at 10 m with a horizontal resolution of ~ 55 km. Here we calculate daily average wind vectors and
212 re-grid to the 25-km EASE-grid.

213 *d. Bathymetric Depth: International Bathymetric Chart of the Arctic Ocean (IBCAO)*

214 We use bathymetric depth from IBCAO (Jakobsson et al. 2020) for comparisons of model
215 performance after training. We make use of the Version 4.2 product without elevation data for the
216 Greenland Ice Sheet on a $400\text{ m} \times 400\text{ m}$ grid cell spacing, re-gridded to the 25-km EASE-grid.

217 **4. Methods**

218 *a. Model Inputs*

219 We employ a suite of machine learning and statistical models (PS, LR, and CNN) to predict
220 present-day sea-ice velocity components ($u_{i,t}$ & $v_{i,t}$) using the input parameters:

- 221 • present-day zonal & meridional wind velocity ($u_{a,t}$ & $v_{a,t}$),
- 222 • previous-day zonal & meridional sea-ice velocity ($u_{i,t-1}$ & $v_{i,t-1}$), and
- 223 • previous-day sea-ice concentration (c_{t-1}).

224 Inputs are chosen based on results from Zhai and Bitz (2021), who showed that the above
225 combination of parameters produced skillful output when used to predict sea-ice motion with a
226 CNN. Sea-ice velocity might be expected to be dependent also on sea-ice thickness, in addition to
227 our selected input fields (Hibler 1979; Thorndike and Colony 1982). However, feature exploration
228 studies of CNN models applied to Community Earth System Model version 2 (CESM2) output
229 by Zhai and Bitz (2021) found that the inclusion of sea-ice thickness as an input parameter does
230 not greatly impact the overall skill and correlation of CNN predictions. Fortunately the thickness
231 is not an important input, as satellite observations of sea-ice thickness prior to 2019 have a high
232 uncertainty, are discontinuous in time and unavailable during the summer. Therefore this parameter
233 is omitted from our analyses. We note that efforts are being made to extend the CryoSat-2 sea-ice
234 thickness record back in time using machine learning techniques (Landy et al. 2022). However,
235 these data are available bi-weekly and thus do not meet the requirements of this study for daily
236 data.

237 Inputs are taken from satellite and reanalysis sources listed in section 3. All variables are
238 normalized to zero mean and one standard deviation before being input into the models, based
239 on the global statistics of the entire record used here from 1989-2021. Data are broken up into

240 train, validation and test data sets with an 88%–6%–6% split (e.g. train with years 1989–2017,
 241 validate with years 2018–2019 and test with years 2020–2021). The train, validate, and test years
 242 are shuffled ten times to produce data for ten different ensemble runs for each ML model. We refer
 243 to an “ensemble run” as a run that is trained on a different temporal subset of data. We calculate
 244 performance statistics (discussed in section 4.c) for each ensemble run and average over the ten
 245 runs for final results. A CNN requires inputs to be of consistent size, with consistent spatial and
 246 temporal coverage, and without non-numerical (e.g. not-a-number or ‘NaN’) values. Thus, while it
 247 may make sense to remove data in regions where sea-ice motion data are not available (i.e. sea-ice
 248 concentration is zero or there is land) before training, due to the practical constraints of applying a
 249 CNN sea-ice velocity components are set to zero during training. A time-variable mask is used to
 250 remove these sea ice free points during model evaluation. Additionally, while uncertainty metrics
 251 are available for the Polar Pathfinder sea-ice motion product, we do not mask out any points during
 252 training due to the constraints of CNN models listed above. We note that taking uncertainty into
 253 account during training of PS and LR models is possible, but to maintain consistency between
 254 models we leave that for future work.

255 *b. Model Setup*

256 We compare prediction outputs from three different models: PS, LR, and CNN.

257 1) PERSISTENCE AND LINEAR REGRESSION MODELS

258 PS predicts the present-day sea-ice velocity to be the same as the previous day at each grid point
 259 (Equation 2):

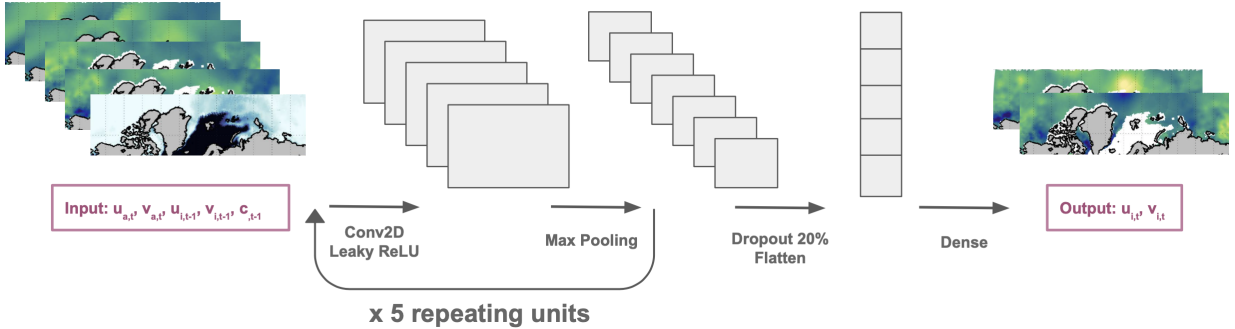
$$u_{i,t}^* = u_{i,t-1}^*. \quad (2)$$

260 This offers a baseline measure of the variability of the system and of the minimum skill that any
 261 alternative models should attain. Here the vector u_i^* is a complex number, where the real and
 262 imaginary parts are the zonal and meridional components of the sea-ice velocity vector.

263 LR regresses each of the five input parameters (section 4.a) onto the sea-ice velocity components
 264 (Equation 3):

$$u_{i,t}^* = Au_{a,t}^* + Bu_{i,t-1}^* + Cc_{i,t-1}^* + D \quad (3)$$

265 Given inputs and outputs, LR solves for parameters A to D . In equation (3), A to D are complex
 266 constants, and the vectors u_i^* , u_a^* and c_i^* are complex numbers, where the imaginary part of c_i^* is set
 267 to zero. LR is carried out in two different manners: one is performed globally (LR-g), and uses each
 268 time snapshot as an independent sample for fitting, providing one equation for the entire modeled
 269 region in the Arctic; the other is performed grid-wise (LR), leading to a different regression
 270 equation for each grid point. For both LR configurations we employ ridge regression with a ridge
 271 parameter of $\lambda = 10^{-2}$ to limit the magnitude of the regression coefficients and prevent them from
 272 being unrealistically large (Marquardt and Snee 1975). The value of the ridge parameter is chosen
 273 based on the iterative approach in Marquardt and Snee (1975) where we make step changes from
 274 small to large values of λ and pick the value of λ for which the LR coefficients stabilize (i.e. are not
 275 infinitely large). We also note that data are not removed from the training set when $c_i = 0$, which
 276 may dampen the wind dependence in LR because the model is trained that $u_i = 0$ when $u_a \neq 0$ in
 277 these locations. As discussed in section 4.a, these data are not masked during training because the
 278 CNN requires numerical values (i.e. not ‘NaN’).



279 FIG. 2. Schematic of the convolutional neural network (CNN) used in this study for predicting present-day
 280 sea-ice velocity components, $u_{i,t}$ & $v_{i,t}$ (outputs), from present-day wind velocity, $u_{a,t}$ & $v_{a,t}$, previous-day
 281 sea-ice velocity, $u_{i,t-1}$ & $v_{i,t-1}$, and previous-day sea-ice concentration, $c_{i,t-1}$ (inputs). This CNN has five
 282 repeating units of a 2D convolution with a ReLU activation and max pooling, followed by a 20% dropout layer,
 283 flattening and a dense layer.

284 2) CONVOLUTIONAL NEURAL NETWORK (CNN) ARCHITECTURE

285 A CNN is a type of ML model typically applied to visual images, where a computer is fed
 286 numerous (hundreds to millions) different images and learns from their patterns in order to make

287 a prediction (O’Shea and Nash 2015). We use data sets that are image-like in that they have a
 288 specified value at various grid-points on a map (for images this would be colors at various pixel
 289 locations). Incorporation of spatial information when making predictions is one of the benefits of
 290 CNN over LR or PS models, in addition to the ability of a CNN to capture non-linearities in the
 291 relationships between the input predictors and the outputs. Our CNN (Fig. 2) is set up with five
 292 repetitions of the block unit: 2D convolution, ReLU (Rectified Linear Unit), and 2D max-pooling.
 293 This is followed by a 20% drop-out layer, a flattening to a one-dimensional vector, and finally a
 294 regression onto a 1D vector (dense layer) representative of the output predictions. This output is
 295 then concatenated into two maps of present-day zonal and meridional sea-ice velocity.

296 We implement the CNN in python using the Tensorflow/Keras library (Abadi et al. 2015).
 297 Convolutional and ReLU layers are carried out with (1,1) strides and (3,3) filter sizes, whereas the
 298 max pooling strides and filter sizes are (2,2). For each of the respective repeating block units, there
 299 are 7, 14, 28, 56, and 112 filters. The training runs for 50 epochs with a batch size of 365 days.
 300 Optimization is carried out with an Adam optimizer and a normalized root mean squared error as
 301 the loss function (second term in Equation 5 discussed below). Similarly to the LR, we employ
 302 ridge regression with a ridge parameter of $\lambda = 10^{-2}$. Further descriptions of the architectural
 303 components of a CNN (i.e. layers, strides, filters, ReLU, max pooling, etc.) can be found in
 304 O’Shea and Nash (2015). Filter sizes are chosen based on the conventional VGGNet architecture
 305 (Szegedy et al. 2015). We do not carry out hyperparameter tuning for this study in order to maintain
 306 consistency with the architecture of Zhai and Bitz (2021), with the only differences being in the
 307 sizes and number of the filters due to differences in the sizes of the starting input maps.

308 *c. Model Evaluation*

309 As in Zhai and Bitz (2021), the model performances are evaluated and compared based on the
 310 correlation (Corr) and skill, given by:

$$corr_{x,y} = \frac{\sum_i^n (x_i - \bar{x})(y_i - \bar{y})}{\sqrt{\sum_i^n (x_i - \bar{x})^2} \sqrt{\sum_i^n (y_i - \bar{y})^2}}, \quad (4)$$

$$skill_{x,y} = 1 - \frac{\sqrt{(x_i - y_i)^2}}{\sqrt{(x_i - \bar{x})^2}}, \quad (5)$$

311 where x represents observations, and y represents predicted values of a sample size n . The
 312 correlation (Equation 4) is defined as the covariance between prediction and observation scaled by
 313 their standard deviations. The skill (Equation 5) is a representation of the fraction of the observed
 314 standard deviation explained by the model predictions, where the second term is the root mean
 315 squared error normalized by the standard deviation of the observations (Thomson and Emery
 316 2014). The correlation ranges from -1 to 1, with 1 indicating a perfect positive relationship, -1
 317 indicating a perfect negative relationship, and zero representing orthogonality. The skill can range
 318 from negative infinity to 1, with 1 representing a perfect match between model predictions and
 319 observations. The correlation is a measure of how well the phase variability in the data is explained
 320 by the model, whereas the skill is a measure of the absolute error in the model predictions.

321 These metrics are calculated using the test data set (varying years, as discussed in section 4.a)
 322 of which the models have no prior knowledge. Two different masks are made and both applied
 323 to the data during model evaluation: one is time-variable and evaluates model outputs only at
 324 times and in locations where sea-ice concentration is greater than zero; the other is constant with
 325 time and masks out all areas where sea-ice concentration is zero more than 20% of the time from
 326 1992–2017. Metrics are calculated overall (section 5.a.1), at each grid point to provide spatial
 327 evaluation (section 5.a.2), over each month for temporal evaluation (section 5.a.3), and for different
 328 percentile ranges of various sea-ice properties (wind speed, ice speed, and ice concentration) to
 329 understand the role these play on the model performance (section 5.a.4). For temporal evaluations
 330 we calculate the monthly mean for each of the ten ensemble runs. Overall monthly means are then
 331 represented by the mean of the ten ensemble runs, and monthly errors are calculated as the standard
 332 error of the mean of the ten ensemble runs (as discussed in section 4.a). Temporal evaluations are
 333 carried out for for different regions within the Arctic. The divisions (Fig. 1a) are made based on
 334 spatial distributions of model performance metrics ($corr_{CNN}$ and $corr_{CNN} - corr_{LR}$ in Fig. 3c & f),
 335 representing regions of: (i) variable model performance and LR greatly outperforming CNN (i.e.
 336 variable $corr_{CNN}$ and $corr_{LR} \gg corr_{CNN}$; Greenland Sea, dark blue), (ii) low model performance
 337 and LR slightly outperforming CNN (i.e. low $corr_{CNN}$ and $corr_{LR} > corr_{CNN}$; Eastern Arctic,

338 light blue), (iii) high model performance and CNN slightly outperforming LR (ie. high $corr_{CNN}$
339 and $corr_{LR} < corr_{CNN}$; Central Arctic, light red), and (iv) variable model performance and CNN
340 greatly outperforming LR (i.e. variable $corr_{CNN}$ and $corr_{LR} \ll corr_{CNN}$; Baffin Bay, dark red).

341 *d. Model Comparison*

342 We also investigate the correlation and skill differences between the LR and CNN models,
343 which requires an understanding of where the differences are significant. Significance tests on the
344 differences are approximated with a cross-validated t test (Dietterich 1998; Tang et al. 2000). The
345 cross-validated t test proceeds as follows: (i) for each of the ten ensemble runs, the correlation and
346 skill for the LR and CNN are calculated for each grid point or percentile range for a given variable
347 and transformed by Fisher’s z transform (Equation 14.5.6 in Press et al. 1986) to remove skewness
348 in the distribution; (ii) the difference between the transformed correlation and skill for the two
349 models is calculated and averaged over the ten ensemble runs; (iii) a two-tailed t test is performed
350 to detect whether the mean difference between the two models is significantly different from zero
351 at the 95% confidence level. The cross-validated t test uses the degrees of freedom to calculate
352 significance. For spatial comparisons (section 5.a.2) we estimate degrees of freedom using the
353 temporal decorrelation scale to estimate the number of independent time series of sea-ice motion
354 in the Arctic. This temporal decorrelation scale is taken as the e -folding scale of a Gaussian fit to
355 the autocorrelation of the sea-ice speed calculated at different time-lags (Equations 10 and 11 in
356 Sumata et al. 2018).

357 *e. Analysis of Inputs*

358 We analyze the spatial and temporal variability of different parameters related to ice motion
359 (wind speed, u_a ; ice speed, u_i ; and ice concentration, c_i) to assess how the model performance
360 compares to the model inputs. Spatial analyses look at maps of the average and standard deviation
361 of each parameter over time from 1989–2021. This type of analysis is useful for comparing these
362 properties to maps of the model performance metrics in order to understand different regimes
363 within the Arctic. We also look at the seasonality of each of these properties. Similarly to the
364 input analysis in section 4.c, monthly errors are calculated as the standard error of the mean of the

365 ten ensemble runs, and temporal evaluations are carried out for different divisions that are chosen
366 based on the model performances.

367 **5. Results**

368 *a. Model Performance*

369 1) OVERALL

370 We evaluate the overall performance of the different models by calculating the correlation and
371 skill over all gridpoints and times (Table 1). The CNN has the highest correlation and skill,
372 followed closely by the grid-wise linear regression (LR). The grid-wise LR largely outperforms the
373 global LR (LR-g) that covers the entire Arctic, which is not much better than the simple PS model.
374 These results confirm the advantage of using a model that captures non-linearity (CNN) and the
375 heterogeneity of Arctic sea ice motion statistics (both CNN and LR). The better performance of
376 the CNN, LR, and LR-g models in comparison to the PS confirms that sea-ice motion depends on
377 wind and sea-ice concentration on daily time scales. Table 1 shows the pattern that an increase
378 in model complexity leads to an increase in performance. Additionally, because correlation is a
379 measure of how well the model is able to capture the phasing, while skill measures the model's
380 ability to capture phasing and magnitude, the high correlation but lower skill suggests the models
381 do well capturing the phasing but incur error in capturing the magnitude.

Model	Correlation	Skill
Persistence (PS)	0.69 ± 0.02	0.21 ± 0.02
Linear Regression, global (LR-g)	0.72 ± 0.01	0.30 ± 0.01
Linear Regression, gridwise (LR)	0.78 ± 0.02	0.37 ± 0.02
Convolutional Neural Network (CNN)	0.81 ± 0.01	0.42 ± 0.02

382 TABLE 1. Overall correlation and skill between observations and predictions of sea-ice velocity for four
383 different models.

384 2) SPATIAL

385 Spatial variations in the correlation (Fig. 3) and skill (not shown) are similar for the PS, LR,
386 and CNN models. Models perform well for predictions in the central Arctic, with decreasing
387 performance in coastal locations. Low values of correlation (Fig. 3a–c) are visible in the Bering
388 Strait, Bering Sea, Hudson Bay, East Siberian Sea, Laptev Sea, Kara Sea, and off the coast of

389 Greenland. Particularly poor model performances are found near the islands in the Eastern Arctic.
390 The best model performance is seen north of Fram Strait and in the Beaufort Sea.

391 Typically, $corr_{CNN} > corr_{LR} > corr_{PS}$, similar to the results from section 5.a.1. The spatial
392 differences in correlation between the models are shown in Fig. 3d–f. Regions in red indicate areas
393 where the first model in the difference metric outperforms the second (i.e. $corr_{CNN} > corr_{PS}$ in
394 Fig. 3d, $corr_{LR} > corr_{PS}$ in Fig. 3e, and $corr_{CNN} > corr_{LR}$ in Fig. 3f), whereas blue regions
395 indicate the opposite (i.e. $corr_{CNN} < corr_{LR}$ in Fig. 3f). Gray regions show where the difference
396 in correlation between the two models is not statistically significant. The CNN and LR models
397 outperform the PS over the entire Arctic (Fig. 3d & e), with the exception of the western side of
398 Baffin Bay where the PS outperforms the LR (blue). Overwhelmingly, the CNN outperforms the
399 LR (red in Fig. 3f). Interestingly, the LR has a higher correlation (blue) in coastal regions where
400 both models have decreased performance (i.e. near the islands in the Eastern Arctic and off the
401 coast of Greenland).

402 The spatial patterns in model performance compared to the distance from the coast are confirmed
403 in Fig. 4. Correlations for the CNN and LR models tend to be lower in coastal regions (Fig. 4a–b).
404 This is also true for skill (not shown). For both models, locations that are greater than 400 km
405 from the coast consistently have correlation greater than 0.7 (and skill greater than 0.3, not shown).
406 The finding that the CNN outperforms the LR model for most cases is confirmed in Fig. 4c, where
407 most of the data lie in the positive region (i.e. above the black line). Conversely, locations where
408 the LR outperforms the CNN only occur within 400 km of the coast.

409 We also show that models have decreased performance in shallower regions (Fig. 4d–e). Overall,
410 model performance increases with increasing seafloor depth. The relationship is logarithmic:
411 performance increases rapidly with increasing depth for depths shallower than 1000 m, while the
412 trend levels out for depths greater than 1000 m. Models exhibit correlations less than 0.7 and 0.5
413 (CNN and LR, respectively) only for locations with depths less than 1000 m. The CNN outperforms
414 the LR for most cases (Fig. 4f). Most regions where the LR outperforms the CNN (below the black
415 line) occur at depths shallower than 500 m, although there are some instances of higher correlation
416 of the LR for greater depths.

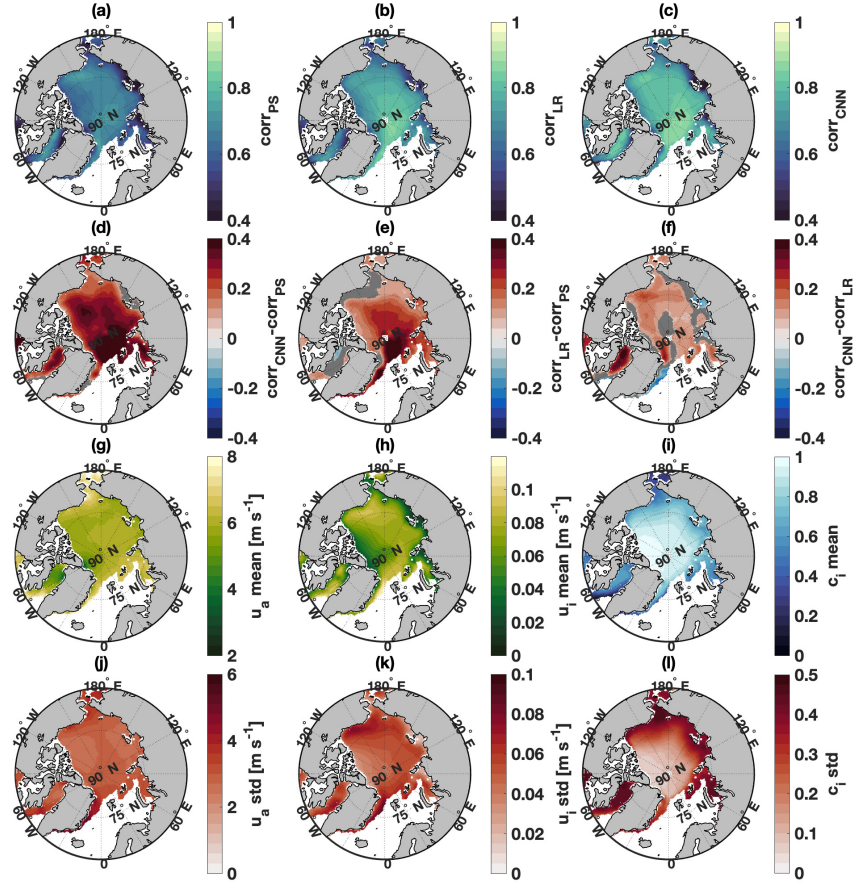
417 We also analyze the spatial variability of the various properties related to sea-ice motion (wind
418 speed, u_a ; sea-ice speed, u_i ; and sea-ice concentration, c_i). The mean and standard deviation of

419 the properties listed above are mapped in Fig. 3g–l. Patterns in mean ice speeds tend to coincide
420 with the spatial patterns in wind speed (Fig. 3 g & h), consistent with the known dependence of
421 ice motion on wind speed (Thorndike and Colony 1982). Both ice and wind speed are relatively
422 low in the coastal and island regions of the East Siberian Sea, the Canadian Arctic Archipelago,
423 and off the northern and western coasts of Greenland. The highest mean wind speeds occur in the
424 Davis Strait, off the eastern coast of Greenland, and in the Bering Strait; high mean ice speeds also
425 occur in these regions, in addition to the Beaufort Sea. The region of low mean ice speeds to the
426 north of the Canadian Arctic Archipelago coincides with high mean ice concentrations (Fig. 3h &
427 i). Conversely, the region of low mean ice speeds in the East Siberian Sea coincides with lower
428 mean ice concentrations.

429 Regions that show high variability (large standard deviations) in ice speed coincide with high
430 mean ice speeds (i.e. in the Beaufort Sea, Baffin Bay, Davis Strait, and Greenland Sea), while
431 regions with low variability coincide with lower mean ice speeds (to the north of the Canadian
432 Arctic Archipelago and in the East Siberian sea) (Fig. 3 h & k). Variability in wind speed is found
433 to be relatively consistent throughout the Arctic, with the exception of high variability off the
434 eastern coast of Greenland (Fig. 3j). Regions with large variability in ice concentration typically
435 correspond to regions with lower mean ice concentrations (i.e. in the East Siberian Sea, Baffin Bay,
436 the Kara Sea, and the Bering Strait). These are the regions where the largest amount of seasonal
437 ice melt typically occurs (not shown), which contributes to the large variability and lower mean
438 ice concentrations.

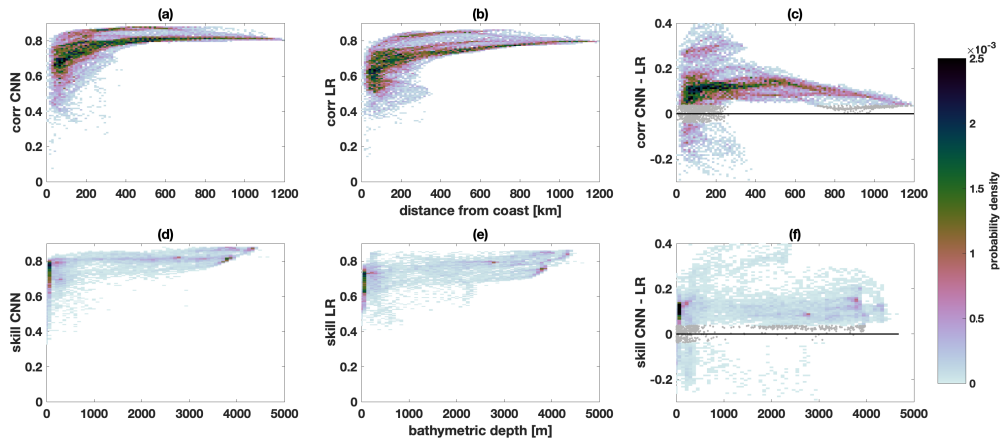
449 3) TEMPORAL

450 For the region containing the entire Arctic, the CNN typically has the highest correlation,
451 followed by the LR and then the PS model (Fig. 5a). During June–September the difference in
452 correlation between the CNN and LR models is not statistically significant. Temporal structure is
453 visible in the correlation for all of the models. The LR model performance (Fig. 5a) has a larger
454 range of seasonal variability than the other two models. Maximum correlation and skill for the PS
455 and CNN models occurs during October–December, while the LR has a correlation maximum in
456 June–August. All three models experience a minimum performance in April.



439 FIG. 3. (a–c) Mapped correlation for predictions of sea-ice velocity made by the (a) PS, (b) LR, and (c) CNN
 440 models. (d–f) The difference in correlation between models: (d) $corr_{CNN} - corr_{PS}$, (e) $corr_{LR} - corr_{PS}$, and (f)
 441 $corr_{CNN} - corr_{LR}$. The gray regions in d–f represent locations where the difference in correlation between the
 442 two models is not statistically significant. (g–i) Mean and (j–l) standard deviation in time of various properties
 443 related to sea-ice motion from satellite and reanalysis products (wind speed, u_a (g & j); sea-ice speed, u_i (h & k);
 444 and sea-ice concentration, c_i (i & l)).

457 The temporal evaluations are divided into regions (Fig. 1a) based on the spatial variability of
 458 their performance, as discussed in section 4.c. The impacts of this spatial division on model
 459 performance are shown in Fig. 5b–d, while Fig. 5e–g represent differences in the correlation
 460 between the different models. Here the black lines represent metrics calculated with all of the data
 461 included, and the different shades of red and blue represent the respective spatial regions from
 462 Fig. 1a. Diamonds in Fig. 5e–g indicate months where the difference between the two models is
 463 statistically significant. The correlation for the region within the Central Arctic division (light red)



445 FIG. 4. PDFs for model performances compared to their distance from the coast (a–c) and bathymetric depth
 446 (d–f), with (a & d) for the CNN and (b & e) for the LR. (c & f) The difference ($corr_{CNN} - corr_{LR}$) between the
 447 correlation of the two models. Gray shading (c & f) represents correlation differences between the two models
 448 that are not statistically significant. Results for skill (not shown) are similar to correlation.

464 does not deviate much from that of the entire Arctic (black) because the Central Arctic region is
 465 large and covers most of the region containing the entire Arctic. However, there are significant
 466 changes in monthly values of correlation for all other divisions (Greenland Sea, Eastern Arctic,
 467 and Baffin Bay divisions). For all three models, the Eastern Arctic (light blue) division exhibits a
 468 similar seasonal cycle to the entire Arctic (i.e. minimum correlation in March–April), but has a
 469 consistently lower monthly correlation in comparison to the other divisions for all models, except
 470 during the months of July–October.

471 The Greenland Sea (dark blue) and Baffin Bay (dark red) divisions exhibit a relatively high
 472 correlation from October–May that decreases toward a minimum in August or September (Fig. 5b–
 473 d). The Greenland Sea division (dark blue) has a higher correlation than the other divisions from
 474 October–April for all three models. The Greenland Sea division shows a lower correlation than
 475 the region containing the entire Arctic from the months of June–September, reaching a minimum
 476 in August for all three models that is significantly lower than correlations for the entire Arctic (i.e.
 477 the CNN has a minimum of 0.54 for the Greenland Sea division in comparison to 0.80 for the
 478 overall Arctic). The Baffin Bay division (dark red) exhibits the largest deviations in correlation
 479 from the overall Arctic for all models, showing up as a large decrease during the months of May–
 480 November. The Baffin Bay division has higher correlations in December–April, and the lowest

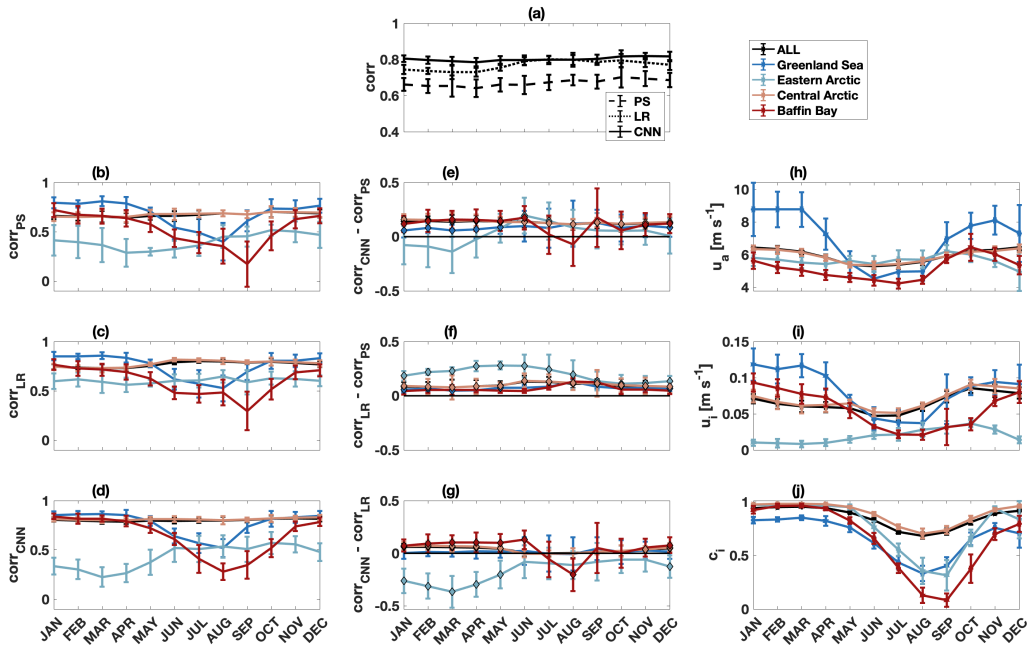
481 August–September minimum out of all of the divisions for all models (i.e. the August correlation
482 of the CNN within the Baffin Bay division is 0.28 in comparison to 0.80 for the entire Arctic).
483 The performance minima that occur in August–September for the Greenland Sea and Baffin Bay
484 regions are much lower than the April minima for the region containing the entire Arctic. This
485 pattern of decreased model performance during months of minimum sea-ice extent (Greenland Sea
486 and Baffin Bay divisions) suggests a link between model performance and sea-ice concentration,
487 which will be further evaluated in section 5.c.

488 The differences in correlation between the models for the different divisions are shown in
489 Fig. 5e–g. The LR and CNN typically outperform the PS for all divisions (i.e. diamonds indicating
490 statistically significant difference in model performance are above zero in Fig. 5e & f). The LR
491 outperforms the CNN in all months for the Eastern Arctic division. However, statistically significant
492 differences from zero are only present December–May. The CNN outperforms the LR during the
493 months of September–May for the Central Arctic, and September–June for the Baffin Bay division.
494 However, the difference between the correlation of the CNN and LR is not statistically significant
495 during the months of June–October for the Central Arctic or July and September–November for
496 the Baffin Bay division. These differences in model correlation will be further analyzed in section
497 5.c.

498 We also compare the temporal variability in performance to that of the various properties related
499 to sea-ice motion (wind speed, u_a ; sea-ice speed, u_i ; and sea-ice concentration, c_i). The ensemble
500 mean monthly averages of various properties related to sea-ice motion are shown in Fig. 5h–j.
501 Analysis is further broken down into the four divisions within the Arctic, which are chosen based
502 on values of the model correlations (Fig. 1).

503 For all regions the seasonal cycles for ice speed and wind speed (Fig. 5h & i) generally line up,
504 with minima typically occurring during the summer months and maxima in the winter. The seasonal
505 pattern of minimum wind speeds occurring from June–July, and maximum speeds anywhere from
506 October–February is consistent throughout all regions, except for the Eastern Arctic division where
507 minima are found in December–March, and maxima occur in September–October. The Greenland
508 Sea division has greater seasonal variability in wind and ice speeds than the other divisions,
509 with comparatively high maximum speeds in November–April. Seasonal patterns in ice speed
510 show minima in June–July for the Central Arctic, June–August for the Greenland Sea, and May–

511 October for the Baffin Bay division. The Eastern Arctic division shows the opposite seasonal trend,
 512 instead exhibiting minimum ice speed from December–May. Sea-ice concentration also follows a
 513 seasonal cycle within each division, typically reaching a maximum in March and a minimum in
 514 September (Fig. 5j). The Baffin Bay division exhibits the lowest and longest duration minimum ice
 515 concentration (i.e. $c_i < 0.5$ from July–October). From December–May the Greenland Sea division
 516 has a lower ice concentration than the other divisions, which are all similar during this time.



517 FIG. 5. (a–d) Ensemble mean monthly correlation for the prediction of sea-ice velocity by three different
 518 models: (a) all models, (b) persistence, (c) linear regression, and (d) CNN. (e–g) The difference between the
 519 correlation of the (e) CNN and PS, (f) LR and PS, and (g) CNN and LR models. (h–j) Ensemble mean monthly
 520 values of various properties related to sea-ice motion (wind speed, u_a (h); sea-ice speed, u_i (i); and sea-ice
 521 concentration, c_i (j)). Metrics are calculated for five different regions: containing the entire area of the Arctic
 522 (black), and within the spatial divisions indicated in Fig. 1a (shades of red and blue). Error bars represent
 523 ensemble mean standard deviations. Diamonds in Fig. 5e–g indicate months where the difference between the
 524 two models represented is statistically significant.

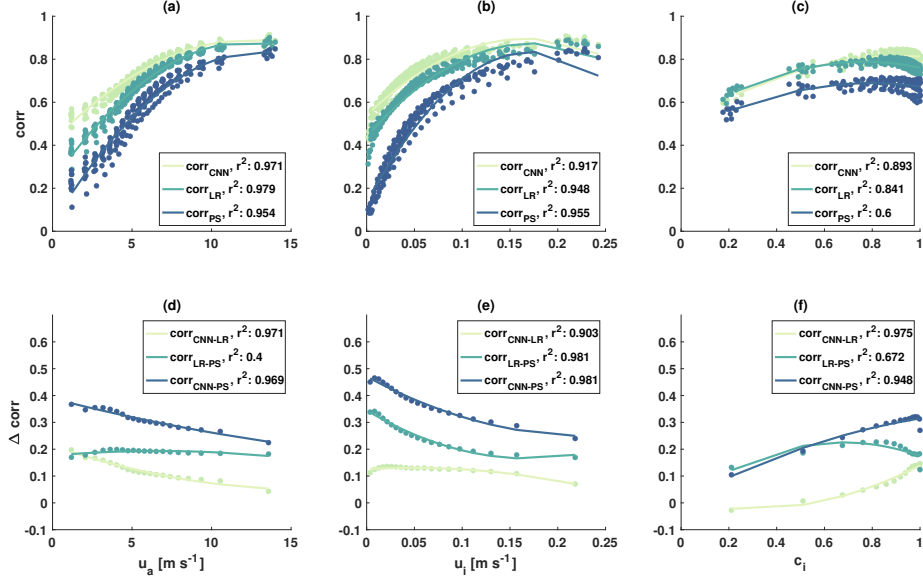
525 4) MODEL PERFORMANCE FOR PERCENTILES OF INPUTS

526 The model performance is compared to properties related to sea-ice motion (wind speed, u_a ;
527 sea-ice speed, u_i ; and sea-ice concentration, c_i) to probe the variability in model correlation in
528 space and time. Figure 6 shows the correlation metrics calculated from subsets of test data for all
529 models (PS in dark blue, LR in teal, and CNN in green). Subdivisions are based on percentile
530 ranges (5% intervals) of the various properties. The performance metrics (correlation (a–c) and
531 the difference in correlation between the various models (d–f)) are plotted against the average of
532 each percentile range (i.e. 0–5%, 5–10%, etc.) for each property. Skill metrics (not shown) have
533 similar patterns to the correlation. We find that the correlation increases with increasing wind
534 speed, sea-ice speed, and sea-ice concentration for all models (Fig. 6a–c). These relationships
535 have statistically significant r^2 values when fit to a second-order polynomial with a least squares
536 regression.

537 The CNN and LR consistently outperform the PS model, as these two difference metrics
538 ($corr_{CNN-corr_{PS}}$ & $corr_{LR-corr_{PS}}$) are positive for all u_a , u_i , and c_i (blue and teal lines in
539 Fig. 6 d–f). The CNN has a higher correlation than the LR (green lines in Fig. 6 d–f), except for the
540 case where $c_i < 0.5$ (Fig. 6f). The metrics for the difference between the CNN and the other two
541 models (i.e. $corr_{CNN-corr_{PS}}$ & $corr_{CNN-corr_{LR}}$) have statistically significant relationships with
542 wind speed, ice speed, and ice concentration: the difference between the two models decreases for
543 increases in wind and ice speed (Fig. 6d & e), and increases with increases in ice concentration
544 (Fig. 6f). The difference metric $corr_{LR-corr_{PS}}$ shows a similar relationship to u_i , but not u_a or c_i .
545 Additionally, the difference between the CNN and the LR is less dependent on u_i than the other
546 two difference metrics (i.e. the slope of the green line is less than the slopes of the teal and blue
547 lines in Fig. 6e). This can be attributed to the correlation of the PS model being much lower than
548 that of the CNN or LR when ice speeds are close to 0 m s^{-1} . The results in Fig. 6d–f are robust
549 whether we use all data or remove non-significant points.

555 *b. Linear Regression Parameters: Relationship Between Sea-Ice Motion and Input Parameters*

556 Analysis of the linear regression parameters provides insight on the locations where each of
557 the inputs is important for predicting sea-ice motion. The parameters from the full LR (A-C in
558 Equation 3) described in section 1 are mapped in Fig. 7. Here Fig. 7a–c represents the magnitude



550 FIG. 6. Correlation of the CNN (a–c) and the difference between CNN and LR correlation (d–f) as a function
 551 of various properties related to sea-ice motion (wind speed, u_a (a & d); sea-ice speed, u_i (b & e); and sea-ice
 552 concentration, c_i (c & f). The correlation is calculated with subsets of test data based on percentiles (5 percent
 553 intervals) of the various parameters. The x-axis represents the mean value of the data in each 5% interval of each
 554 parameter. Correlation differences (d–f) that are not statistically significant are not shown.

559 of the regression coefficients for normalized wind speed, sea-ice speed, and sea-ice concentration
 560 on the sea-ice velocity (i.e. $\sqrt{\Re^2 + \Im^2}$ of A to C , where \Re and \Im represent the real and imaginary
 561 components of these coefficients). These values range between 0 and 1 in the figure because they
 562 are normalized to the maximum overall coefficient. Larger values indicate that sea-ice velocity has
 563 a larger linear dependence on a particular parameter.

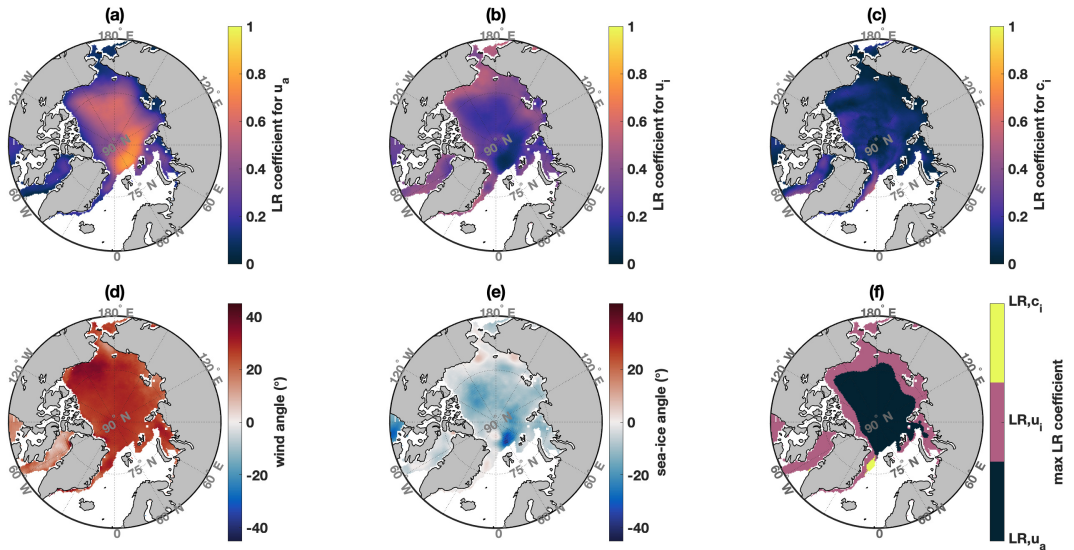
564 Results show that wind speed has the largest importance in predicting sea-ice velocity within
 565 the Central Arctic (Fig. 7a). Near the coast, the LR coefficient for previous-day sea-ice velocity
 566 is elevated (Fig. 7c) complementary to the high values in the interior for wind speed (Fig. 7a).
 567 Fig. 7d–e represents the rotation angles of the wind and sea-ice velocity to the predicted next-day
 568 sea-ice velocity. The wind angle has an average of $24.9^\circ \pm 11.3^\circ$ throughout the Arctic, which is
 569 fully consistent with Nansen’s observations aboard the Fram of angles between 20 and 40° (Ekman
 570 1905), and falls within one standard deviation of previous research (Thorndike and Colony 1982;
 571 Serreze et al. 1989; Maeda et al. 2020) who found wind angles of -5 to 18° , 0 to 19° , and -10 to

572 30° (depending on season; winter to summer), respectively. The spatially averaged angle between
573 present and previous-day sea-ice speed is $-8.3^\circ \pm 6.4^\circ$, with spatial variations as seen in Fig. 7e.
574 When looking at the data, the expected spatial mean of the angle difference between previous and
575 present-day sea-ice velocity is 0.2° (not shown), which is within two standard deviations of the
576 angle found from the LR parameters.

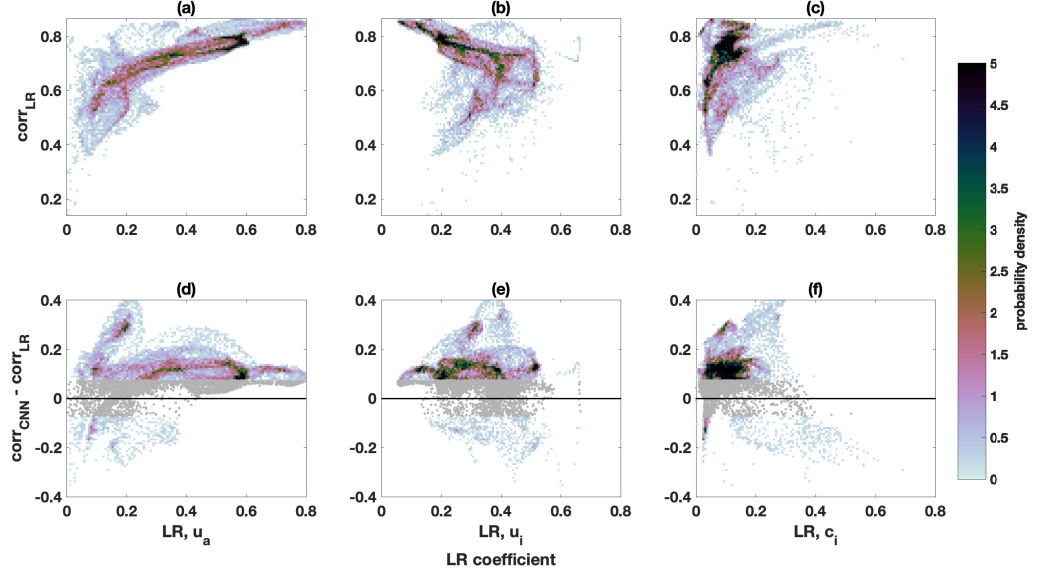
577 Wind velocity is found to have the maximum LR coefficient for predicting sea-ice velocity
578 throughout the Central Arctic (dark blue in Fig. 7f). Locations near the coast are dominated by the
579 sea-ice speed (pink regions). This is consistent with results from previous studies (Thorndike and
580 Colony 1982; Kimura and Wakatsuchi 2000; Maeda et al. 2020) that conclude that the dependence
581 of sea-ice velocity on wind velocity is not as strong in coastal locations where ice stresses become
582 more important. Additionally, the low coefficient for wind velocity found in the Fram Strait off the
583 east coast of Greenland, where the transpolar drift acts as a strong and persistent export pathway
584 for Arctic sea-ice (Weiss 2013), has previously been attributed to strong surface ocean currents
585 (Kimura and Wakatsuchi 2000).

586 The LR coefficient for wind speed is related to the spatial patterns in the mean c_i (Figs. 7a &
587 3i). We find low values for the LR parameter for wind speed in the Canadian Arctic Archipelago,
588 a region where c_i is high and has little temporal variability (Fig. 3i &l), which is consistent
589 with results from Kimura and Wakatsuchi (2000); Maeda et al. (2020). However, regions of low
590 mean c_i often have smaller values for the LR wind coefficient (i.e. coastal regions in the eastern
591 Arctic, Baffin Bay, and the Bering Strait). This contradicts results from Kimura and Wakatsuchi
592 (2000); Maeda et al. (2020), where areas with high ice concentration exhibit a relatively small wind
593 factor as a result of internal stresses becoming more important in regions where ice is thick and
594 concentrated. However, we note that in contrast to Kimura and Wakatsuchi (2000), our model also
595 includes u_i as a predictor, which increases in importance near the coast. Additionally, our analysis
596 has one LR coefficient at each spatial location throughout all time from 1992–2017, which provides
597 a description of the relationship between the wind factor and the average c_i at each location. In
598 contrast, Maeda et al. (2020) have a different LR equation for each month, providing a better picture
599 of the relationship between the wind factor and the instantaneous c_i , which is more likely to display
600 impacts of ice stresses.

601 Values of the LR coefficients are related to the performance of the LR model and to the difference
 602 between the CNN and LR model performance. Figure 8 shows the relationship between the LR
 603 coefficients and the model correlation (Fig. 7a–c), and the difference between the correlation of
 604 the CNN and the LR (Fig. 7d–e), as calculated at each grid point. Larger LR coefficients for wind
 605 speed are associated with larger correlation of the LR model (Fig. 8a) in addition to an improved
 606 performance of the CNN over the LR (Fig. 8d). Conversely, a larger LR coefficient for sea-ice
 607 speed is associated with lower correlation (Fig. 8b) and does not show a statistically significant
 608 relationship with the difference metric, $corr_{CNN} - corr_{LR}$ (Fig. 8e). A larger LR parameter for ice
 609 concentration is linked to higher model correlation (Fig. 8c) and tends toward the LR outperforming
 610 the CNN (Fig. 8f). The skill (not shown) exhibits the same patterns as the correlation.



611 FIG. 7. (a–c) Magnitude of the normalized linear regression coefficient for the relationship between sea-ice
 612 velocity components and input parameters (a, wind speed, A ; b, sea-ice speed, B ; c, sea-ice concentration, C)
 613 normalized to the maximum of a–c. (d–e) Mean angle of (d) wind speed and (e) sea-ice speed to the predicted
 614 next-day sea-ice speed. (f) Maximum linear regression parameter (a–c) for predicting sea-ice velocity at each
 615 location. Wind and ice speed parameters are derived from calculating the magnitude of the parameters for the
 616 velocity components.



617 FIG. 8. PDFs for LR correlation (a–c) and the difference between the correlation of the CNN & LR correlation
 618 (d–f) compared to the LR coefficient magnitudes for (a & d) wind speed, LRu_a ; (b & e) sea-ice speed, LRu_i ;
 619 and (c & f) sea-ice concentration, LRc_i .

620 *c. Attribution assessment of model predictive skill*

621 We address our aims to understand (i) reductions in forecast skill and (ii) discrepancies in the
 622 performance of the different models by comparing the variability of these performance metrics (i.e.
 623 $corr_{CNN}$ and $corr_{CNN} - corr_{LR}$) to variables related to ice motion (i.e. distance from coast, d_c ;
 624 bathymetric depth, d ; wind speed, u_a ; ice speed, u_i ; ice concentration, c_i ; and the LR coefficients
 625 for wind speed, A , ice speed, B , and ice concentration, C). We focus on the difference between the
 626 CNN and the LR, because the CNN and LR both outperform the PS for almost all spatial locations.

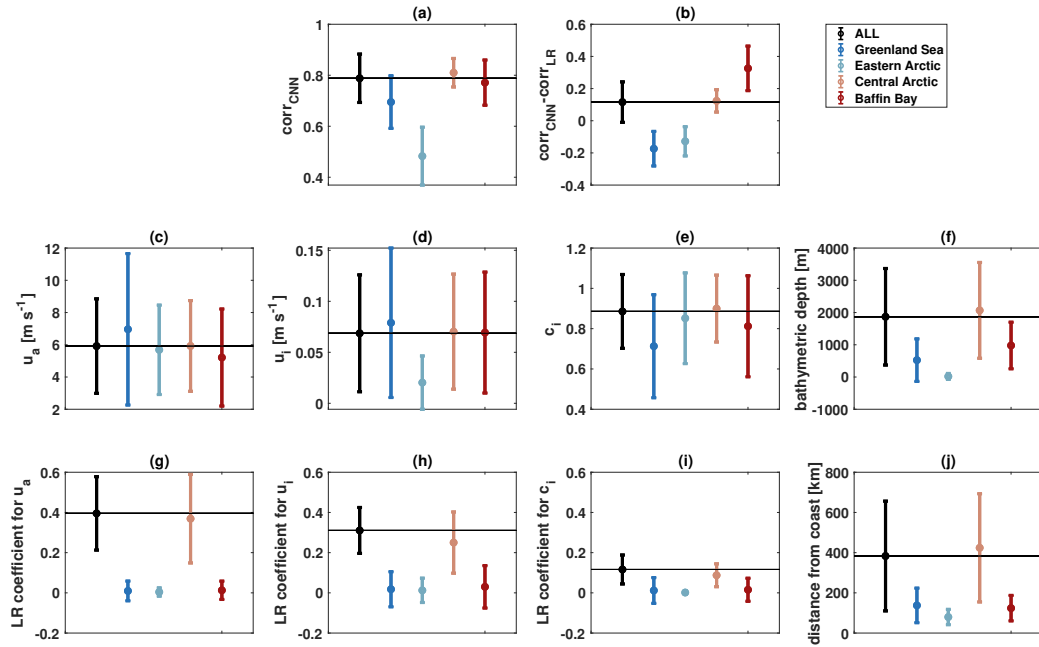
627 In section 5 we find high model performance is linked to large distances from the coast, depths
 628 (Fig. 4 in section 5.a.2), wind speed, ice speed, ice concentration, (Fig. 6 in section 5.a.4), and values
 629 of the LR coefficients for wind speed & ice concentration (Fig. 8 in section 5.b). Additionally,
 630 the difference between the correlation of the CNN and LR models is typically smaller for high
 631 wind speed and ice speed, and larger for high sea-ice concentration (Fig. 6d–f in section 5.a.4),
 632 large distances from the coast, and large depths (Fig. 4 in section 5.a.2). We aim to confirm these
 633 findings by comparing the spatial and temporal variability in model correlation (Figs. 3a–f & 5a–g)

634 to that of the various properties linked to ice motion (Figs. 3g–l & 5h–j), as well as to the spatial
635 variability of the LR coefficients (Fig. 7a–c).

636 We analyze four spatial divisions (Fig. 1a) that are made based on overall model performance and
637 the difference between the performance of the CNN and LR models. The Greenland Sea division
638 (dark blue in Fig. 1a) covers the region to the east of Greenland where the model correlation
639 is variable, but the LR largely outperforms the CNN. The Eastern Arctic division (light blue
640 in Fig. 1a) represents the region of the eastern Arctic where the correlation is low and the LR
641 outperforms the CNN. The Central Arctic division (light red in Fig. 1a) includes the central Arctic,
642 the Beaufort Sea, and the regions to the north of the Canadian Arctic Archipelago. The Baffin
643 Bay division (dark red in Fig. 1a) is the region where the model correlation is variable, but the
644 CNN consistently outperforms the LR. The gray shading in Fig. 1a indicates regions that are
645 not included in the following analysis. We discuss how the variability in the input parameters is
646 linked to (i) model performance, (ii) the difference between the performance of the CNN and LR
647 models, and (iii) the values for the LR coefficients in each division. We note the distinction between
648 inter-divisional comparisons and analysis within each division, both of which are discussed below.

649 A summary of the inter-divisional comparisons is shown in Fig 9. Here the average values
650 of the metrics and properties are shown for each division, and error bars represent the standard
651 deviation. While the mean over any given division falls within one standard deviation of the
652 mean for the other division for many properties, significance testing shows that for each property
653 the differences between the mean value for each individual division and all other divisions are
654 statistically significant (not shown). Analysis within each division is summarized in Fig. 10, which
655 shows the ensemble-averaged correlation between each of the performance metrics and each of
656 the properties related to ice motion within each division. The correlation between the maps of the
657 performance metrics (Figs. 3a & f) and the average of the properties throughout time (Figs. 3g–i)
658 are shown in Fig. 10a & b. The correlation between the daily time series of the performance
659 metrics and the spatially averaged properties (similar to Figs. 5d & g vs. Figs. 5h–j, but using
660 daily rather than monthly values) are shown in Fig. 10c & d. The properties are compared to the
661 model correlation (circles, Figs. 10a & c) and the difference between the CNN and LR correlation,
662 $corr_{CNN} - corr_{LR}$ (triangles, Figs. 10b & d). The different divisions are represented by the
663 different colors, as indicated in the legend. Values greater than zero are representative of cases

664 where increases in the property are linked to increases in the model performance metric, while
 665 values less than zero indicate an inverse relationship between the property and performance metric.

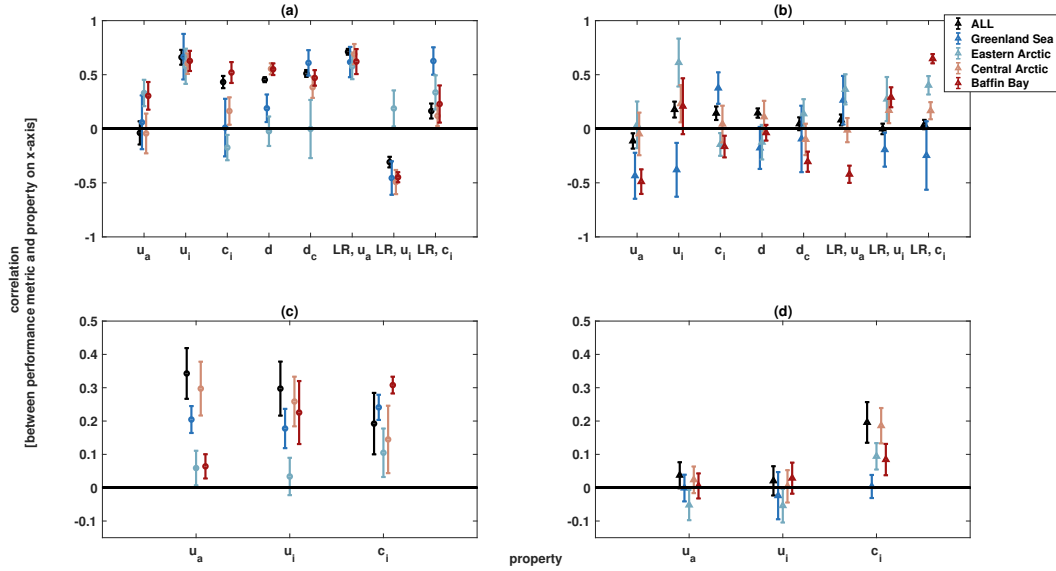


666 FIG. 9. Overall mean of the performance metrics, ((a) $corr_{CNN}$, and (b) $corr_{CNN} - corr_{LR}$), and properties
 667 related to ice motion ((c) wind velocity, u_a ($m s^{-1}$); (d) ice velocity, u_i ($m s^{-1}$); (e) ice concentration, c_i ; (f)
 668 bathymetric depth, d (m); (j) distance from coast, d_c (km); and the LR coefficients for (g) u_a , (h) u_i , and (i)
 669 c_i). Different colors represent the different spatial divisions, as indicated in the legend. Error bars represent the
 670 standard deviation within each division. The black line in panel each represents the mean value for the overall
 671 Arctic ('ALL' in the legend) for comparison.

680 1) MODEL PREDICTIVE SKILL VS. PROPERTIES RELATED TO ICE MOTION

681 Inter-divisional comparisons suggest that low correlation of the CNN is typically linked to low
 682 depth, distance from coast, and ice speed, which is consistent with results from Fig. 6. For example,
 683 the Eastern Arctic division has the lowest $corr_{CNN}$, as well as the lowest mean of the properties
 684 listed above in comparison to the other divisions (Fig 9).

685 Visual inspection of spatial (Fig. 3) and temporal (Fig. 5) results also support this. For example,
 686 the low $corr_{CNN}$ found in the Eastern Arctic division (Fig. 3c) is coincident with low values for
 687 depth, distance from coast (Fig. 1b–c), wind speed, ice speed, and ice concentration (Figs. 3g–i).



672 FIG. 10. Ensemble mean of the correlation between the model performance metrics (circles for $corr_{CNN}$ in
 673 a & c; triangles for $corr_{CNN} - corr_{LR}$ in b & d) and the various properties related to ice motion within each of
 674 the spatial divisions (different shades of red and blue, as indicated in the legend). Correlations are calculated to
 675 understand how (a & b) spatially mapped performance metrics are related to spatial variability in time-averaged
 676 wind speed, u_a ; ice speed, u_i ; ice concentration, c_i ; depth, d ; distance from coast, d_c ; LR parameter for wind,
 677 LRu_a ; LR parameter for ice speed, LRu_i ; and LR parameter for ice concentration, LRc_i ; and (c & d) temporal
 678 variability in performance is linked to daily averages of u_a , u_i , and c_i within each division. Error bars represent
 679 the standard deviation of the ensemble runs within each division.

688 Temporally, the exceptionally low correlation in the Eastern Arctic division from November–May
 689 (Fig. 5b–d) is coincident with values of u_i for the Eastern Arctic division that are lower than all of
 690 the other divisions (Fig 5i). Additionally, the Central Arctic division exhibits a higher correlation
 691 than the other divisions, particularly during May–October, where the Central Arctic has higher u_a ,
 692 u_i and c_i in comparison to the other divisions. Temporal analysis also shows that divisions that
 693 have a lower seasonal minimum c_i also exhibit a lower correlation relative to the other divisions,
 694 and in August–September the ordering for both c_i and $corr_{CNN}$ between divisions is: Baffin
 695 Bay < Eastern Arctic < Greenland Sea < Central Arctic.

696 Within each division, large $corr_{CNN}$ is typically related to high depth, distance from coast, wind
 697 speed, ice speed, and ice concentration, which is consistent with results from Fig. 6. This can

698 be seen in Fig. 10a & c, where data points for all divisions are typically greater than zero (above
699 the black line), which indicates that spatial (Fig. 10a) and temporal (Fig. 10c) variability of the
700 properties listed on the x-axis are linked to variability in the correlation of the CNN. There are
701 a few exceptions to this relationship when comparing spatial variability of performance metrics
702 to the mean field of the properties: large wind speed is linked to low $corr_{CNN}$ within the Central
703 Arctic and the overall Arctic; within the Eastern Arctic division large ice concentration, depth, and
704 distance from coast are linked to low $corr_{CNN}$. Interestingly, many of these exceptions lie within
705 the Eastern Arctic division, where overall depth, distance from coast, wind speed, ice speed, and ice
706 concentration are significantly lower than other divisions. However, the values of these exceptions
707 are within one standard deviation of zero, which indicates neither a positive or negative correlation
708 between the model performance and the respective property. We note that the spatial comparisons
709 (Fig. 10a) make use of the mean fields of u_a , u_i , and c_i , while temporal analyses (Fig. 10c) look at
710 the daily time series that are averaged over the spatial domain of each division. We use spatial and
711 temporal analyses here as a confirmation of results in Fig. 6, but do not expect perfect adherence
712 due to the differences caused by averaging across space and time.

713 While Fig. 10a & c provides a quantitative analysis of the comparisons of spatial (Fig. 3c vs. g–i)
714 and temporal (Fig. 5d vs. h–j) variability in the model correlation with respect to these properties,
715 we can also see the link through visual inspection. For example, spatial patterns of high correlation
716 within the Greenland Sea division (i.e. increasing from west to east; Fig. 3a–c) are coincident
717 with high depth, distance from coast, ice speed, and wind speed, while low correlation is seen in
718 locations with high ice concentration. Within the Eastern Arctic division, low correlation is largely
719 linked to low depth and ice speed (Fig. 10a). High correlation within the Central Arctic division
720 is generally coincident with high depth, distance from coast, ice speed, and ice concentration.
721 Slightly lower correlations are seen in regions with lower values of u_a and u_i (western side), and
722 lower c_i (eastern side and near the Bering Strait). Interestingly, the Beaufort Sea has high values
723 of skill and correlation despite its proximity to land. However, the Beaufort Sea is relatively deep
724 and has exceptionally high mean u_a and u_i in comparison to other coastal regions, properties that
725 are linked to higher model performances (Figs. 4d & 6a–b). Lastly, high model correlation in the
726 Baffin Bay division (Fig. 3) is aligned with large depth (Fig. 1b), u_a , u_i , and c_i (Fig. 3g–i). These
727 spatial patterns of correlation within each of the divisions tend to be consistent with results from

728 Figs. 4d & 6a–b, the main exception being for the link between low correlation and high c_i within
729 the Greenland Sea division, and the high correlation found close to the coast in the Beaufort Sea.

730 Temporally, the seasonal cycle for correlation follows that of u_a , u_i , and c_i , with minimum model
731 correlations occurring during the months of minimum u_a , u_i , and c_i (August–September) for most
732 models and divisions. The exceptions here are the Eastern and Central Arctic divisions where the
733 correlation does not follow the seasonal cycle for c_i . This is likely a result of the low u_a and u_i
734 in the Eastern and Central Arctic division during this time. Additionally, low seasonal variability
735 in correlation within the Central Arctic division could be linked to the relatively small seasonal
736 variations in u_a , u_i , and c_i in comparison to the other divisions.

737 2) DIFFERENCE BETWEEN PREDICTIVE SKILL OF THE CNN AND LR MODELS VS. PROPERTIES RELATED 738 TO ICE MOTION

739 Inter-divisional analysis suggests that low values for the difference metric, $corr_{CNN} - corr_{LR}$
740 (the Greenland Sea and Eastern Arctic divisions in Fig 9b), are linked to low depth, distance from
741 coast, and ice concentration (the Greenland Sea and Eastern Arctic division in Fig 9 e–f & j).
742 Additionally, a low difference metric is linked to high u_a and u_i in the Greenland Sea division.
743 Conversely, low u_i is linked to a low difference metric in the Eastern Arctic division (Fig 9d). The
744 high difference metric in the Baffin Bay division is also linked to a lower mean u_a . As noted above,
745 while the mean value of a particular division may fall within one standard deviation of that for
746 other divisions, significance testing shows that the differences between means among divisions for
747 a given property are statistically significant. For the case of c_i , these inter-divisional comparisons
748 are consistent with results from Fig. 6d–f, where a high difference metric is linked to high c_i .
749 Additionally, these results are consistent with the relationship between high $corr_{CNN} - corr_{LR}$ and
750 low wind and ice speeds found in Fig. 6d–f for the Greenland Sea (u_a & u_i) and Baffin Bay (u_a)
751 divisions, but not the Eastern Arctic division (u_a & u_i).

752 Visual inspection of spatial (Fig. 3f vs. Figs. 1b–c & 3h–j) and temporal (Fig. 5g vs. Fig. 5h–j)
753 results also supports this. Spatially, the low difference metric, $corr_{CNN} - corr_{LR}$, in combination
754 with relatively low depth, distance from coast, ice concentration, and exceptionally high wind and
755 ice speeds in the Greenland Sea division compared to the rest of the Arctic is consistent with
756 results in Fig. 6d–f. Additionally, temporal analysis shows the difference metric for the Greenland

757 Sea division remains lower than that for the entire Arctic (dark blue line is below black line),
758 while u_a and u_i are higher in the Greenland Sea division than other divisions during the months
759 of October–April. Similarly, for the Eastern Arctic division a relatively low depth, distance from
760 coast, and ice concentration are linked to a low difference metric. However, contrary to patterns
761 found in Fig. 6, the difference metric in the Eastern Arctic division is low, while u_a and u_i are also
762 low in both spatial and temporal analyses. The difference metric for the Eastern Arctic division is
763 lower than that for the Greenland Sea division from January–April, despite lower c_i and higher u_a
764 and u_i in the Greenland Sea division, all of which are expected to contribute to a lower difference
765 metric (Fig. 6). Spatially, the high difference metric in the Central Arctic division is linked to
766 high c_i , low u_a , and high u_i relative to other divisions, which is consistent with results in Fig. 6,
767 with the exception of the tendency of u_i . However, in temporal analysis of the Central Arctic
768 division, the difference metric is particularly high compared to other divisions when u_i is lower in
769 January–May, which is consistent with results in Fig. 6. The notably high difference metric in the
770 Baffin Bay division compared to other divisions is linked to low u_a in both spatial and temporal
771 (December–June in Fig. 5g & h) analyses.

772 Within each division, comparisons of $corr_{CNN} - corr_{LR}$ with the properties related to ice motion
773 are more nuanced, as data points in Fig 10b & d do not consistently lie above or below zero for a
774 given property, particularly with spatial comparisons using the mean fields (Fig 10b). From results
775 in Fig. 6, we would expect points in Fig 10b to be above zero for c_i and below zero for u_a and
776 u_i (i.e. high $corr_{CNN} - corr_{LR}$ is linked to high c_i , low u_a , and low u_i), which is only the case
777 for some divisions. The region containing the entire Arctic (black) is consistent with this pattern
778 for all variables on the x -axis, except for u_i . Additionally, these results are consistent with Fig. 6
779 for the following cases: the coincidence of high $corr_{CNN} - corr_{LR}$ with low u_a , low u_i , and high
780 c_i in the Greenland Sea division; high $corr_{CNN} - corr_{LR}$ coincident with low u_a , but high c_i and
781 depth in the Central Arctic region; the coincidence of high $corr_{CNN} - corr_{LR}$ with low u_a in the
782 Baffin Bay region. We find the following exceptions to the trends in Fig. 6: the coincidence of
783 high $corr_{CNN} - corr_{LR}$ and low d and d_c in the Greenland Sea division; high $corr_{CNN} - corr_{LR}$
784 coincident with high u_i and low c_i in the Eastern Arctic division; and high $corr_{CNN} - corr_{LR}$
785 coincident with high u_i , low c_i , low depth, and low distance from coast in the Baffin Bay division.

786 Comparisons between temporal variability of the difference metric and the various properties
787 are more straightforward, and tend to show results that are consistent with what is found in Fig. 6,
788 where a high difference metric is linked to low u_a , low u_i , and high c_i . This is true (i.e. data for u_a
789 and u_i exist below the black line, and points for c_i are above), except for in the case of the region
790 containing the entire Arctic, the Central Arctic division, and the Baffin Bay division for both u_a
791 and u_i , as well as the Greenland Sea division for c_i . Additionally, while the ensemble mean value
792 of the correlation between u_i and the difference metric is negative for the Greenland Sea division,
793 it lies within one standard deviation of zero.

794 Looking at the time series (Fig. 5g–j) it is clear that the low difference metric in the Eastern
795 Arctic division from December–May is linked to low u_i and high c_i , which is the opposite of what
796 is expected from Fig. 6. Within the Central Arctic division low $corr_{CNN} - corr_{LR}$ is linked to
797 low c_i in June–October, while a slightly higher $corr_{CNN} - corr_{LR}$ from December–May is linked
798 to high u_a and low u_i . Within the Baffin Bay division low $corr_{CNN} - corr_{LR}$ is linked to low c_i
799 (Figs. 5g & j & 10d): during months of low c_i , the difference metric is not statistically different
800 from zero (May–November, except August), while for all other months the opposite is true, and
801 $corr_{LR} < corr_{CNN}$. Additionally, high $corr_{CNN} - corr_{LR}$ during January–April is coincident with
802 a low u_a . Temporal results from Fig. 5g–j tend to be consistent with results from Fig. 6, with
803 the following exceptions: coincidence of low $corr_{LR} < corr_{CNN}$ with low u_i and high c_i from
804 December–May within the Eastern Arctic division; coincidence of high $corr_{LR} < corr_{CNN}$ and
805 high u_a from December–May in the Central Arctic division.

806 3) IMPACT OF LR PARAMETERS ON MODEL PERFORMANCE METRICS

807 We find that the performance metrics ($corr_{CNN}$ and $corr_{CNN} - corr_{LR}$) are related to the values
808 of the LR coefficients for the different input parameters (Fig. 8 in section 5.b). These results
809 come from comparing the LR coefficient at each location (Fig. 7a–c) with the mapped values
810 for the performance metrics (Fig. 3c & f). We use divisional analyses to confirm the maximum
811 LR coefficient in each division (Fig. 9g–i vs. Fig. 7f), as well as the relationship between the
812 performance metrics and the LR coefficients within each division (Fig. 10a & b vs. Fig. 8). We also
813 aim to understand whether the variable with the highest LR coefficient has the strongest relationship
814 to model performance. 3.

815 Inter-divisional comparisons (Fig. 9g–i) show that the mean LR coefficient for u_a is higher than
816 all other coefficients in the Central Arctic division and the region covering the entire Arctic. For
817 all other divisions the mean of the LR coefficients are within one standard deviation of each other
818 and the maximum coefficient within each division is not conclusive. The mean LR coefficient
819 within the overall Arctic and the Central Arctic division (Fig. 9g–i) is consistent with what is seen
820 spatially (Fig. 7f). We find that variability in model performance is not necessarily linked most
821 strongly to the property that exhibits the dominant LR coefficient within each division (i.e. a high
822 LR coefficient for u_a does not necessarily mean that the correlation between either performance
823 metric and u_a will be stronger than that between the performance metric and u_i or c_i). In other
824 words, the high value of the LR coefficient for u_a in comparison to that for u_i or c_i for the Central
825 Arctic division in Fig.9g is not linked to the correlation between model performance and u_a being
826 higher than that for u_i or c_i in Fig 10.

827 In Fig. 8, high model correlation is found in locations with large LR coefficient for u_a and c_i ,
828 but a low LR coefficient for u_i . Analysis of the LR coefficient within each division (Fig. 10a & b)
829 confirms this and shows that high $corr_{CNN}$ is related to high a high LR coefficient for u_a and c_i
830 within all four divisions. The relationship between high $corr_{CNN}$ and a low LR coefficient for u_i
831 is also seen for all divisions except the Eastern Arctic division (light blue in Fig. 10a). While the
832 general trend in Fig. 8 suggests high correlation to be linked to a low LR coefficient for u_i , it is
833 clear that when $corr_{CNN} < 0.6$ (which is the case for the Eastern Arctic division, where the mean
834 $corr_{CNN}$ is 0.5 ± 0.02), a high LR coefficient for u_i is linked to higher $corr_{CNN}$.

835 The relationship between a high difference metric and a high LR coefficient for u_a seen in Fig. 8
836 is confirmed within all divisions, except for the Baffin Bay division (Fig. 10b), however the Central
837 Arctic division is within one standard deviation of zero. The relationship between high $corr_{CNN} -$
838 $corr_{LR}$ and a low LR coefficient for c_i seen in Fig. 8c is only found within the Greenland Sea
839 division. While the general pattern in Fig. 8c suggests a link between high $corr_{CNN} - corr_{LR}$ and
840 a low LR coefficient for c_i , this is largely true where the LR coefficient for c_i is high (> 0.6), which
841 is the case for the Greenland Sea division (0.69 ± 0.34). When the LR coefficient for $c_i < 0.6$
842 the opposite is true, and high $corr_{CNN} - corr_{LR}$ is linked to a high LR coefficient for c_i , which is
843 the case for the Greenland Sea, Eastern Arctic, and Baffin Bay divisions. Thus, Fig. 10b confirms
844 results from Fig. 8.

845 **6. Conclusions**

846 *a. A CNN can make skillful predictions of sea-ice motion on one-day time scales.*

847 As sea-ice in the Arctic declines and opens new pathways for maritime transportation, the skill
848 of sea-ice motion predictions becomes increasingly important (Bennett et al. 2020; Cao et al.
849 2022). This work uses machine learning models to make one-day predictions of sea-ice motion
850 for operational forecasting. We show that a CNN can make skillful predictions of sea-ice velocity
851 and outperforms other statistical models in most instances. In comparison to the other models,
852 the CNN has the benefit of incorporating non-linearities between inputs and spatial information
853 when making predictions. We also show that a grid-wise linear regression (LR) model performs
854 almost as well as a CNN in most instances, and comes with the benefit of decreased complexity in
855 comparison to neural networks. Both the CNN and LR models outperform the baseline PS model.
856 Additionally, we find that the CNN shows improved performance in comparison to the models of
857 Maeda et al. (2020); Kimura and Wakatsuchi (2000) discussed in section 2: the correlation of the
858 CNN is as low as 0.4 in the Eastern Arctic, and 0.7 in the Canadian Arctic Archipelago (Fig. 3c),
859 where Maeda et al. (2020) find correlation between ice motion and geostrophic wind as low as 0
860 and 0.4 in the same regions. Lastly, while comparing the model performance to that of a dynamical
861 model was outside the scope of this study, our model was an extension of that presented by Zhai and
862 Bitz (2021) (differences between the two models are identified in Table S1), which was found to
863 have higher correlations for sea-ice velocity with satellite observations than the CICE5 dynamical
864 model for sea ice.

865 *b. Model predictive skill and discrepancies between model performances are linked to various*
866 *properties related to sea-ice motion.*

867 Model performances vary spatially and seasonally, and are linked to variability in properties re-
868 lated to sea-ice motion. Although there are exceptions that come with having different combinations
869 of these properties, in general, better model performance is linked to:

- 870 • increased bathymetric depth and distance from the coast
- 871 • larger mean values of u_a , u_i , and c_i
- 872 • larger LR coefficients for u_a and c_i ; smaller LR coefficient for u_i

873 The CNN outperforms the LR in most cases. We have shown that the following are related to
874 increases in the performance of the CNN over the LR:

- 875 • larger distance from coast and greater bathymetric depth
- 876 • smaller mean u_a and u_i , and larger mean c_i
- 877 • larger LR coefficient for u_a , and smaller LR coefficients for c_i

878 Interestingly, the LR model tends to outperform the CNN model in some coastal regions where
879 non-linear effects might be expected to play a large role. However, the locations where this
880 happens exhibit shallow depths, and when coastal waters are deep (i.e. the Beaufort Sea) the CNN
881 outperforms the LR. We note that sharp discontinuities between ocean and land pixels may reduce
882 the quality of the CNN predictions due to the way the CNN incorporates spatial filters and non-local
883 information in its predictions Sonnewald et al. (2021). This may also impact our result that the LR
884 outperforms the CNN at shallower depths because depth increases with increasing distance from
885 the coast. To address this, future analyses we will apply a non-local LR at each grid-point for a
886 more direct comparison between LR and CNN models. However, even with non-localities built in,
887 the LR doesn't apply spatial filters in the same way that the CNN does, so we may not be able to
888 reproduce the same decreases in performance inherent to the CNN in coastal regions.

889 The LR typically outperforms the CNN in regions where wind speed is not the dominant LR
890 coefficient: ice velocity is the dominant LR coefficient in the coastal regions of the eastern
891 Arctic, and sea-ice concentration dominates the LR predictions in the coastal region to the east of
892 Greenland. Conversely, wind speed is found to be the dominant LR coefficient wherever the CNN
893 outperforms the LR. This suggests that the relationship between wind velocity and ice velocity
894 includes non-linearities that are captured by the CNN (and not the LR), leading to an improved
895 performance.

896 We find that larger LR coefficients for a given parameter are not necessarily linked to larger
897 parameter values (e.g. in the Greenland Sea division, ice concentration is the dominant predictor
898 in regions where wind and ice speed are exceptionally high). However, we find that the LR
899 coefficient for wind speed tends to be lower in regions with low mean c_i . This contradicts previous
900 findings, where areas with high c_i are known to exhibit larger internal ice stresses, which leads to
901 a reduction in the dependence of ice motion on wind (Kimura and Wakatsuchi 2000; Maeda et al.

902 2020). We note that this particular conclusion does not take into account instantaneous effects, as
903 it is a comparison between a mean c_i over time and a LR coefficient that is descriptive of ice motion
904 over the duration of the study. Future work could decrease the time period over which LR is run to
905 obtain equations that are more descriptive of instantaneous effects such as that of ice stresses due
906 to high c_i . Lastly, we find that variability in model performance is not necessarily linked to the
907 dominant LR coefficient within each region.

908 *c. Wind velocity plays the largest role in predicting ice velocity.*

909 We find that the spatial average of the wind factor over the Arctic is 0.72% (Fig. S2). The
910 wind factor is higher for regions in the Central Arctic in comparison to coastal regions, confirming
911 historical results (Thorndike and Colony 1982; Serreze et al. 1989; Kimura and Wakatsuchi 2000;
912 Maeda et al. 2020). We also show an average turning angle to the wind of $24.9^\circ \pm 11.3^\circ$, which is
913 consistent with the cited historical results. Analysis of LR parameters shows that of all of the input
914 predictors, wind velocity has the largest importance in predicting sea-ice velocity. This relationship
915 is particularly strong in the central Arctic, and is reduced in coastal regions. Furthermore, an
916 increased dependence of the models on wind speed is related to increased model performance for
917 the CNN, which provides further evidence as to why the models are not as skillful at predicting
918 ice speed in coastal regions (i.e. ice speed is not as dependent on the training information in
919 these regions). Future work will build off of these results and look at using outputs from machine
920 learning models to understand how the relationship between wind and ice velocity is changing in
921 time as the ice melts.

922 *Acknowledgments.* LH, MRM, and PH were supported by ONR (grant N00014-20-1-2772).
923 MRM was supported by NSF (award OPP-1936222). STG was supported by NSF (award OPP-
924 1936222) and by U.S. Department of Energy (DOE) (Award DE-SC002007). DG was supported
925 by NSF Award 1928305. CMB was supported by NASA (award 80NSSC21K0745). Figures in this
926 report were prepared using MATLAB, Matplotlib: A 2DGraphics Environment Hunter (2007).
927 Colormaps were obtained using the cmocean package (Thyng et al. 2016) and the CubeHelix
928 Colormap Generator (Stephen23 2023). We thank our reviewers for their helpful feedback.

929 *Data availability statement.* We acknowledge all sources of publicly available data that were
930 used in this study. The JRA55-do dataset can be accessed at <https://climate.mri-jma.go.jp/pub/ocean/JRA55-do/>. Polar Pathfinder Daily 25 km EASE-Grid Sea Ice Motion Vectors,
931 Version 4 are made available by the National Snow and Ice Data Center (NSIDC) and can be
932 accessed at <https://nsidc.org/data/nsidc-0116/versions/4>. Sea Ice Concentrations
933 from Nimbus-7 Passive Microwave Data, Version 1 are made available by the NSIDC and can be
934 accessed at <https://doi.org/10.5067/8GQ8LZQVL0VL>. The International Bathymetric Chart
935 of the Arctic Ocean (IBCAO) are available at [https://www.gebco.net/data_and_products/
936 gridded_bathymetry_data/arctic_ocean/](https://www.gebco.net/data_and_products/gridded_bathymetry_data/arctic_ocean/). All of the data and files used for processing for
937 this paper can be accessed at <https://doi.org/10.6075/J0X06774>.
938

939 **References**

- 940 Abadi, M., and Coauthors, 2015: TensorFlow: Large-scale machine learning on heterogeneous sys-
941 tems. URL <https://www.tensorflow.org/>, software available from tensorflow.org, Version 2.8.0.
- 942 Andersson, T. R., and Coauthors, 2021: Seasonal Arctic sea ice forecasting with probabilistic deep
943 learning. *Nature Communications*, **12**, 5124, <https://doi.org/10.1038/s41467-021-25257-4>.
- 944 Bennett, M. M., S. R. Stephenson, K. Yang, M. T. Bravo, and B. De Jonghe, 2020: The opening
945 of the transpolar sea route: Logistical, geopolitical, environmental, and socioeconomic impacts.
946 *Marine Policy*, **73**, 104 178, <https://doi.org/10.1016/j.marpol.2020.104178>.
- 947 Blanchard-Wrigglesworth, E., R. Cullather, W. Wang, J. Zhang, and C. Bitz, 2015: Model forecast
948 skill and sensitivity to initial conditions in the seasonal sea ice outlook. *Geophysical Research
949 Letters*, **42** (19), 8042–8048, <https://doi.org/10.1002/2015GL065860>.

- 950 Brodzik, M. J., B. Billingsley, T. Haran, B. Raup, and M. H. Savoie, 2012: Ease-grid 2.0: Incremental but significant improvements for earth-gridded data sets. *ISPRS International Journal of Geo-Information*, **1** (1), 32–45, URL <https://www.mdpi.com/2220-9964/1/1/32>.
- 951
952
- 953 Cao, Y., and Coauthors, 2022: Trans-arctic shipping routes expanding faster than the model predictions. *Global Environmental Change*, **73**, 102 488, <https://doi.org/10.1016/j.gloenvcha.2022.102488>.
- 954
955
- 956 Carmack, E., and Coauthors, 2015: Toward quantifying the increasing role of oceanic heat in sea ice loss in the new Arctic. *Bulletin of the American Meteorological Society*, **96** (12), 2079–2105, <https://doi.org/10.1175/BAMS-D-13-00177.1>.
- 957
958
- 959 Cavalieri, D., C. Parkinson, P. Gloersen, and H. Zwally, 1996: Sea ice concentrations from Nimbus-7 SMMR and DMSP SSM/I-SSMIS Passive Microwave Data, Version 1. NASA National Snow and Ice Data Center Distributed Active Archive Center, URL <https://nsidc.org/data/NSIDC-0051/versions/1>, access Date: March 2021.
- 960
961
962
- 963 Crawford, A., J. Stroeve, A. Smith, and A. Jahn, 2021: Arctic open-water periods are projected to lengthen dramatically by 2100. *Communications Earth & Environment*, **2** (1), 109, <https://doi.org/10.1038/s43247-021-00183-x>.
- 964
965
- 966 Dietterich, T., 1998: Approximate statistical tests for comparing supervised classification learning algorithms. *Neural Computation*, **10**, 1895–1923, <https://doi.org/10.1162/089976698300017197>.
- 967
968
- 969 Dumitru, C. O., V. Andrei, G. Schwarz, and M. Datcu, 2019: Machine learning for sea ice monitoring from satellites. *The International Archives of the Photogrammetry, Remote Sensing and Spatial Information Sciences*, **XLII-2/W16**, 83–89, <https://doi.org/10.5194/isprs-archives-XLII-2-W16-83-2019>.
- 970
971
- 972 Ekman, W. V., 1905: On the influence of the earth's rotation on ocean-currents. *Arkiv for Matematik, Astronomi Och Fysik*, **2** (11), 1–52.
- 973
- 974 Feltham, D. L., 2008: Sea ice rheology. *Annual Review of Fluid Mechanics*, **40** (1), 91–112, <https://doi.org/10.1146/annurev.fluid.40.111406.102151>.
- 975
- 976 Hibler, W., 1979: A dynamic thermodynamic sea ice model. *Journal of Physical Oceanography*, **9** (4), 815–846, [https://doi.org/10.1175/1520-0485\(1979\)0090815:ADTSIM2.0.CO;2](https://doi.org/10.1175/1520-0485(1979)0090815:ADTSIM2.0.CO;2).
- 977

- 978 Hoffman, L., M. R. Mazloff, S. T. Gille, D. Giglio, C. M. Bitz, P. Heimbach, and K. Matsuyoshi,
979 2023: Data from: Machine learning for daily forecasts of arctic sea-ice motion: an attribution
980 assessment of model predictive skill. UC San Diego Library Digital Collections., publish Data:
981 June 2023, <https://doi.org/10.6075/J0X06774>.
- 982 Hsieh, W. W., and B. Tang, 1998: Applying neural network models to prediction and data analysis
983 in meteorology and oceanography. *Bulletin of the American Meteorological Society*, **79 (9)**, 1855
984 – 1870, [https://doi.org/10.1175/1520-0477\(1998\)079<1855:ANNMTP>2.0.CO;2](https://doi.org/10.1175/1520-0477(1998)079<1855:ANNMTP>2.0.CO;2).
- 985 Hunke, E., and Coauthors, 2020: Should sea-ice modeling tools designed for climate research be
986 used for short-term forecasting? *Current Climate Change Reports*, **6**, 121–136, <https://doi.org/10.1007/s40641-020-00162-y>.
- 987
- 988 Hunter, J. D., 2007: Matplotlib: A 2d graphics environment. *Computing in Science & Engineering*,
989 **9 (3)**, 90–95, <https://doi.org/10.1109/MCSE.2007.55>.
- 990 Jahn, A., 2018: Reduced probability of ice-free summers for 1.5°C compared to 2°C warming.
991 *Nature Climate Change*, **8**, 409–413, <https://doi.org/10.1038/s41558-018-0127-8>.
- 992 Jakobsson, M., L. Mayer, C. Bringensparr, and et al., 2020: The international bathymetric chart of
993 the arctic ocean version 4.0. *Sci Data*, **7 (176)**, <https://doi.org/10.1038/s41597-020-0520-9>.
- 994 Kern, S., T. Lavergne, D. Notz, L. T. Pedersen, R. T. Tonboe, R. Saldo, and A. M. Sørensen,
995 2019: Satellite passive microwave sea-ice concentration data set intercomparison: closed ice
996 and ship-based observations. *The Cryosphere*, **13 (12)**, 3261–3307, <https://doi.org/10.5194/tc-13-3261-2019>.
- 997
- 998 Kim, Y. J., H.-C. Kim, D. Han, S. Lee, and J. Im, 2020: Prediction of monthly arctic sea ice
999 concentrations using satellite and reanalysis data based on convolutional neural networks. *The*
1000 *Cryosphere*, **14 (3)**, 1083–1104, <https://doi.org/10.5194/tc-14-1083-2020>.
- 1001 Kimura, N., and M. Wakatsuchi, 2000: Relationship between sea-ice motion and geostrophic wind
1002 in the northern hemisphere. *Geophysical Research Letters*, **27 (22)**, 3735–3738, <https://doi.org/10.1029/2000GL011495>.
- 1003

- 1004 Kobayashi, S., and Coauthors, 2015: The jra-55 reanalysis: General specifications and basic char-
1005 acteristics. *Journal of the Meteorological Society of Japan. Ser. II*, **93** (1), 5–48, [https://doi.org/](https://doi.org/10.2151/jmsj.2015-001)
1006 10.2151/jmsj.2015-001.
- 1007 Kwok, R., G. Spreen, and S. Pang, 2013: Arctic sea ice circulation and drift speed: Decadal
1008 trends and ocean currents. *Journal of Geophysical Research: Oceans*, **118** (5), 2408–2425,
1009 <https://doi.org/https://doi.org/10.1002/jgrc.20191>.
- 1010 Landy, J., G. Dawson, and M. Tsamados, 2022: A year-round satellite sea-ice thickness record
1011 from cryosat-2. *Nature*, **609**, 517–522, <https://doi.org/10.1038/s41586-022-05058-5>.
- 1012 Lee, S., J. Im, J. Kim, M. Kim, M. Shin, H.-c. Kim, and L. J. Quackenbush, 2016: Arctic sea ice
1013 thickness estimation from cryosat-2 satellite data using machine learning-based lead detection.
1014 *Remote Sensing*, **8** (9), <https://doi.org/10.3390/rs8090698>.
- 1015 Li, M., R. Zhang, and K. Liu, 2021: Machine learning incorporated with causal analysis for
1016 short-term prediction of sea-ice. *Frontiers in Marine Science*, **8** (649378), [https://doi.org/10.](https://doi.org/10.3389/fmars.2021.649378)
1017 3389/fmars.2021.649378.
- 1018 Maeda, K., N. Kimura, and H. Yamaguchi, 2020: Temporal and spatial change in the relationship
1019 between sea-ice motion and wind in the arctic. *Polar Research*, **39**, [https://doi.org/10.33265/](https://doi.org/10.33265/polar.v39.3370)
1020 polar.v39.3370.
- 1021 Marquardt, D. W., and R. D. Snee, 1975: Ridge regression in practice. *The American Statistician*,
1022 **29** (1), 3–20, <https://doi.org/10.1080/00031305.1975.10479105>.
- 1023 Maykut, G., A. Thorndike, and N. Untersteiner, 1972: Aidx scientific plan. *AIDJEX Bulletin*, **15**,
1024 1–67.
- 1025 McGovern, A., R. Lagerquist, D. J. Gagne, G. E. Jergensen, K. L. Elmore, C. R. Homeyer, and
1026 T. Smith, 2019: Making the black box more transparent: Understanding the physical implications
1027 of machine learning. *Bulletin of the American Meteorological Society*, **100** (11), 2175 – 2199,
1028 <https://doi.org/10.1175/BAMS-D-18-0195.1>.
- 1029 Meredith, M., and Coauthors, 2019: Chapter 3: Polar regions. in: IPCC special report on the
1030 ocean and cryosphere in a changing climate.

- 1031 Notz, D., and J. Stroeve, 2018: The trajectory towards a seasonally ice-free arctic ocean. *Current*
1032 *Climate Change Reports*, **4**, 407–416, <https://doi.org/10.1007/s40641-018-0113-2>.
- 1033 Olason, E., and D. Notz, 2014: Drivers of variability in Arctic sea-ice drift speed. *Journal of*
1034 *Geophysical Research: Oceans*, **119** (9), 5755–5775, <https://doi.org/10.1002/2014JC009897>.
- 1035 Onarheim, I. H., T. Eldevik, L. H. Smedsrud, and J. Stroeve, 2018: Seasonal and regional
1036 manifestation of arctic sea ice loss. *Journal of Climate*, **13** (12), 4917–4932, <https://doi.org/10.1175/JCLI-D-17-0427.1>.
- 1038 O’Shea, K., and R. Nash, 2015: An introduction to convolutional neural networks. arXiv,
1039 <https://doi.org/10.48550/ARXIV.1511.08458>.
- 1040 Petrou, Z. I., and Y. Tian, 2019: Prediction of sea ice motion with convolutional long short-term
1041 memory networks. *IEEE Transactions on Geoscience and Remote Sensing*, **57** (9), <https://doi.org/10.1109/TGRS.2019.2909057>.
- 1043 Press, W., B. Flannery, S. Teukolsky, and W. Vetterling, 1986: *Numerical Recipes*. Cambridge
1044 University Press, 636-639 pp.
- 1045 Rampal, P., J. Weiss, and D. Marsan, 2009: Positive trend in the mean speed and deformation rate of
1046 arctic sea ice, 1979-2007. *Journal of Geophysical Research*, **114** (C5), C05 013, <https://doi.org/10.1029/2008JC005066>.
- 1048 Serreze, M. C., R. G. Barry, and A. S. McLaren, 1989: Seasonal variations in sea ice motion and
1049 effects on sea ice concentration in the canada basin. *Journal of Geophysical Research: Oceans*,
1050 **94** (C8), 10 955–10 970, <https://doi.org/10.1029/JC094iC08p10955>.
- 1051 Serreze, M. C., M. M. Holland, and J. Stroeve, 2007: Perspectives on the arctic’s shrinking ice
1052 cover. *Science*, **315** (5815), 1533–1536, <https://doi.org/10.1126/science.1139426>.
- 1053 Sonnewald, M., R. Lguensat, D. C. Jones, P. D. Deuben, J. Brajard, and V. Balaji, 2021: Bridging
1054 observations, theory and numerical simulation of the ocean using machine learning. *Environ-*
1055 *mental Research Letters*, **16** (073008), <https://doi.org/10.1088/1748-9326/ac0eb0>.
- 1056 Stephen23, 2023: Cubehelix colormap generator: Beautiful and versatile! GitHub, URL <https://github.com/DrosteEffect/CubeHelix/releases/tag/2.3.2>,
1057 access Date: January 2023.

- 1058 Stroeve, J., and D. Notz, 2018: Changing state of arctic sea ice across all seasons. *Environmental*
1059 *Research Letters*, **13** (10), 103 001, <https://doi.org/10.1088/1748-9326/aade56>.
- 1060 Stroeve, J., M. C. Serreze, M. M. Holland, J. E. Kay, J. Malanik, and A. P. Barrett, 2012: The
1061 Arctic's rapidly shrinking sea ice cover: A research synthesis. *Climate Change*, **110**, 1005–1027,
1062 <https://doi.org/10.1007/s10584-011-0101-1>.
- 1063 Sumata, H., and Coauthors, 2018: Decorrelation scales for arctic ocean hydrography – part i:
1064 Amerasian basin. *Ocean Science*, **14** (1), 161–185, <https://doi.org/10.5194/os-14-161-2018>.
- 1065 Szegedy, C., and Coauthors, 2015: Going deeper with convolutions. *2015 IEEE Conference on*
1066 *Computer Vision and Pattern Recognition (CVPR)*, 1–9, [https://doi.org/10.1109/CVPR.2015.](https://doi.org/10.1109/CVPR.2015.7298594)
1067 [7298594](https://doi.org/10.1109/CVPR.2015.7298594).
- 1068 Taboda, F. F., C. A. Stock, S. M. Griffies, J. Dunne, J. G. John, J. R. Small, and H. Tsujino, 2019:
1069 Surface winds from atmospheric reanalysis lead to contrasting oceanic forcing and coastal
1070 upwelling patterns. *Ocean Modelling*, **133**, 79–111, [https://doi.org/10.1016/j.ocemod.2018.11.](https://doi.org/10.1016/j.ocemod.2018.11.003)
1071 [003](https://doi.org/10.1016/j.ocemod.2018.11.003).
- 1072 Tang, B., W. W. Hsieh, A. H. Monahan, and F. T. Tangang, 2000: Skill comparisons between neural
1073 networks and canonical correlation analysis in predicting the equatorial pacific sea surface
1074 temperatures. *Journal of Climate*, **13** (1), 287–293, [https://doi.org/10.1175/1520-0442\(2000\)](https://doi.org/10.1175/1520-0442(2000)013<0287:SCBNNA>2.0.CO;2)
1075 [013<0287:SCBNNA>2.0.CO;2](https://doi.org/10.1175/1520-0442(2000)013<0287:SCBNNA>2.0.CO;2).
- 1076 Thoman, R. L., and Coauthors, 2022: The arctic. *Bulletin of the American Meteorological Society*,
1077 **103** (8), S257 – S306, <https://doi.org/https://doi.org/10.1175/BAMS-D-22-0082.1>, URL <https://journals.ametsoc.org/view/journals/bams/103/8/BAMS-D-22-0082.1.xml>.
- 1079 Thomson, R. E., and W. J. Emery, 2014: *Statistical Methods and Error Handling*. Data Analysis
1080 Methods in Physical Oceanography (Third Edition), Elsevier, 219-311 pp., [https://doi.org/10.](https://doi.org/10.1016/B978-0-12-387782-6.00003-X)
1081 [1016/B978-0-12-387782-6.00003-X](https://doi.org/10.1016/B978-0-12-387782-6.00003-X).
- 1082 Thorndike, A., and R. Colony, 1982: Sea ice motion in response to geostrophic winds.
1083 *Journal of Geophysical Research: Oceans*, **87** (C8), 5845–5852, [https://doi.org/10.1029/](https://doi.org/10.1029/JC087iC08p05845)
1084 [JC087iC08p05845](https://doi.org/10.1029/JC087iC08p05845).

- 1085 Thyng, K. M., C. A. Greene, R. D. Hetland, H. M. Zimmerle, and S. F. DiMarco, 2016: True colors
1086 of oceanography: Guidelines for effective and accurate colormap selection. *Oceanography*,
1087 **29** (3), <https://doi.org/10.5670/oceanog.2016.66>.
- 1088 Toms, B. A., E. A. Barnes, and I. Ebert-Uphott, 2020: Physically interpretable neural networks
1089 for the geosciences: Applications to earth system variability. *Journal of Advances in Modeling*
1090 *Earth Systems*, **12** (9), e2019MS002 002, <https://doi.org/10.1029/2019MS002002>.
- 1091 Tschudi, M., W. Meier, J. Stewart, C. Fowler, and J. Maslanik, 2019: Polar Pathfinder Daily 25
1092 km EASE-Grid Sea Ice Motion Vectors, Version 4. NASA National Snow and Ice Data Center
1093 Distributed Active Archive Center, URL <https://nsidc.org/data/NSIDC-0116/versions/4>, access
1094 Data: March 2021.
- 1095 Tschudi, M. A., W. N. Meier, and J. S. Steward, 2020: An enhancement to sea ice motion and
1096 age products at the National Snow and Ice Data Center (NSIDC). *The Cryosphere*, **14** (5),
1097 1519–1536, <https://doi.org/10.5194/tc-14-1519-2020>.
- 1098 Tsujino, H., and Coauthors, 2018: JRA-55 based surface dataset for driving ocean–sea-ice models
1099 (JRA55-do). *Ocean Modelling*, **130**, 79–139, <https://doi.org/10.1016/j.ocemod.2018.07.002>.
- 1100 Untersteiner, N., A. Thorndike, D. Rothrock, and K. Hunkins, 2007: AIDJEX Revisited: A
1101 look back at the U.S.-Canadian Arctic Ice Dynamics Joint Experiment 1970-78. *Arctic*, **60** (3),
1102 327–336, URL <http://www.jstor.org/stable/40512908>.
- 1103 Wang, X., R. Chen, C. Li, Z. Chen, F. Hui, and X. Cheng, 2022: An intercomparison of
1104 satellite derived Arctic sea ice motion products. *Remote Sensing*, **14** (5), [https://doi.org/](https://doi.org/10.3390/rs14051261)
1105 [10.3390/rs14051261](https://doi.org/10.3390/rs14051261).
- 1106 Weiss, J., 2013: *Drift, Deformation, and Fracture of Sea Ice: A Perspective Across Scales*. Springer
1107 Dordrecht, <https://doi.org/10.1007/978-94-007-6202-2>.
- 1108 Zhai, J., and C. M. Bitz, 2021: A machine learning model of Arctic sea ice motions. [https://doi.org/](https://doi.org/10.48550/ARXIV.2108.10925)
1109 [10.48550/ARXIV.2108.10925](https://doi.org/10.48550/ARXIV.2108.10925).